

OPEN JOURNAL OF

NANAN



ISSN:2147-0081

Volume:8, Issue: 2, Year: 2023

A JOURNAL ABOUT
NANOSCIENCE

Open Journal of Nano

Editor in Chief

Dr. Mustafa CAN, Sakarya University of Applied Sciences, Turkey

mustafacan@subu.edu.tr

Editorial Board

Dr. Mithat ÇELEBİ, Yalova University,
Turkey.

mithat.celebi@yalova.edu.tr

Dr. Hamza ŞİMŞİR, Karabuk University,
Turkey.

hamzasimsir@karabuk.edu.tr

Dr. Harun GÜL, Sakarya University of
Applied Sciences, Turkey.

harungul@subu.edu.tr

Dr. Mustafa Zahid YILDIZ, Sakarya
University of Applied Sciences, Turkey.

mustafayildiz@sakarya.edu.tr

Dr. Numan GÖZÜBENLİ, Harran
University, Turkey.

gnuman@harran.edu.tr

Dr. Oğuz SARIBIYIK, Gümüşhane
University, Gumushane, Turkey.

oysaribiyik@gumushane.edu.tr

Dr. Tuğrul ÇETİNKAYA, Sakarya
University, Turkey.

tcetinkaya@sakarya.edu.tr

Dr. Niyaz Mohammad MAHMOODI
Institute for Color Science and Technology,
Iran.

mahmoodi@icrc.ac.ir

Dr. Gang Andy SHI
Rice University, USA.

gshi@rice.edu

Dr. Abdülkadir KIZILASLAN,
Sakarya University, Sakarya, Turkey.

akizilaslan@sakarya.edu.tr

Dr. Emrah ÖZAKAR, Ataturk University,
Erzurum, Turkey.

emrahozakar@atauni.edu.tr

Dr. Zafer Ömer ÖZDEMİR
University of Health Sciences
Istanbul, Turkey.

emrahozakar@atauni.edu.tr

Field Editors

Dr. Hasan HACİFAZLIOĞLU, İstanbul
University-Cerrahpaşa, İstanbul, Turkey.

hasanh@istanbul.edu.tr

Dr. Erol ALVER, Hitit University, Turkey.

erolalver@hitit.edu.tr

Dr. Kamal YUSOH, University Malaysia
Pahang, Malaysia.

kamal@ump.edu.my

Dr. Tetiana TEPLA, Lviv Polytechnic
National University, Ukraine.

tetiana.l.tepla@lpnu.ua

Dr. Deniz ŞAHİN, Gazi University, Turkey.

dennokalk@hotmail.com

Dr. Menekşe SAKİR,
Erciyes University,
Nanotechnology Application and Research
Center, Erzurum, Turkey.

meneksesarihan@erciyes.edu.tr

Dr. Birgül BENLİ, İstanbul Technical
University, Turkey.

benli@itu.edu.tr

Field Editors

Dr. Mümin Mehmet KOÇ,
Kırklareli University,
Kırklareli, Turkey.
muminmehmetkoc@klu.edu.tr

Dr. Raşit Fikret YILMAZ,
National Defence University, Istanbul,
Turkey.
rasitfikretyilmaz@gmail.com

Dr. İrem DENİZ,
Manisa Celal Bayar University, Manisa,
Turkey.
iremdenz@gmail.com

Dr. Mahmut YILDIZ,
Gebze Technical University,
Kocaeli, Turkey.
yildizm@gtu.edu.tr

Dr. Mehmet Berat TAŞKIN,
Leibniz Institute for Polymer Research,
Dresden, Germany.
berattaskin@gmail.com

Dr. Maria Taj Muhammad,
Jinnah University for Women,
Karachi, Pakistan.
maariaataj@gmail.com

Dr. Mohamed Mahmoud NASEF,
Universiti Teknologi Malaysia Kuala
Lumpur, Kuala Lumpur, Malaysia.
mahmoudeithar@mailcity.com,
mahmoudeithar@cheme.utm.my

Dr. Ramzi KHIARI,
Higher Institute of Technological Studies in
Ksar-Hellal, Ksar-Hellal, Tunisia.
khiari_ramzi2000@yahoo.fr

Statistics Editor

Dr. Özer UYGUN, Sakarya University,
Sakarya, Turkey.
ouygun@sakarya.edu.tr

Language Editors

Dr. Yasin AKGÜL,
Karabuk University, Turkey.
yasinakgul@karabuk.edu.tr

Dr. Tuğrul ÇETİNKAYA,
Sakarya University, Turkey.
tcetinkaya@sakarya.edu.tr

Dr. Abdülkadir KIZILASLAN,
Sakarya University, Sakarya, Turkey.
akizilaslan@sakarya.edu.tr

Dr. Mehmet Berat TAŞKIN,
Leibniz Institute for Polymer Research,
Dresden, Germany.
berattaskin@gmail.com

Dr. Maria Taj Muhammad,
Jinnah University for Women,
Karachi, Pakistan.
maariaataj@gmail.com

Open Journal of Nano

Editorial Assistants

Mücahid SARI, Sakarya University of Applied Sciences, Sakarya, Turkey.

<https://dergipark.org.tr/en/pub/@mucahidsari>

Engin Deniz PARLAR, Sakarya University of Applied Sciences, Sakarya, Turkey. denizparlar-97@hotmail.com

Nadir ATMACA, The Istanbul Metropolitan Municipality, Istanbul, Turkey.

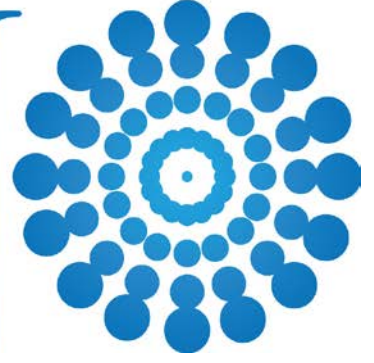
nadiratmaca@gmail.com

Halid ÖZGÜR, FreshForty Media, Turkey

halid@freshforty.media

Enis AKSOY, Areya illüstrasyon, Sakarya, Turkey

enisaksoy@gmail.com



Contents

Volume: 8, Issue: 2, Year: 2023

The inhibitory activity of Ruxolitinib against COVID-19 major protease enzyme and SARS CoV-2 spike glycoprotein: A molecular docking study 65-73
(Research Article)

A. Demet DEMİRAG, Sefa ÇELİK, Samet ARSLAN, Ayşen ÖZEL, Sevim AKYÜZ

The Effect of 1-hydroxybenzotriazole on the Decolorization of Anthraquinone and Diazo Dyes Using Peroxidase Enzyme 74-83
(Research Article)

Mithat ÇELEBİ, Melda ALTIKATOĞLU

Effect of Different Passivation Treatments on Alkali Zn-Ni Coatings: Corrosion Resistance and Adhesion Performance of Geomet 321 and ML Black Coatings 84-98
(Research Article)

İbrahim USTA, Oğuz YILMAZ, Minel GÜL, Ahmet CAN, Harun GÜL

Al-5Ti-0,2B ve Al-5Ti-1B Tane İncelticilerin AA 1050 Alüminyum Alaşımının Mekanik Özellikleri Üzerine Etkileri 99-106
(Araştırma Makalesi)

Tuğçe YUNAK, Erhan DURU, Samet SEVİNÇ, Serdar ASLAN

Investigation of the Effect of Huntit Filler on Flame Retardancy and Mechanical Properties of Silicone Rubber-based Materials in Cable Applications 107-116
(Research Article)

Halil Can UĞRAŞKAN, Fatma Sevde DUMAN, Serkan EMİK

The Inhibitory Activity of Ruxolitinib Against COVID-19 Major Protease Enzyme and SARS Cov-2 Spike Glycoprotein: A Molecular Docking Study

* ¹Aliye Demet Demirag , ²Sefa Celik , ³Samet Arslan , ²Aysen E. Ozel , ⁴Sevim Akyuz 

¹ Yeditepe University, Vocational School, Internet and Network Technologies Department, Istanbul, 34755, Turkiye.

² Istanbul University, Faculty of Science, Department of Physics, Vezneciler, Istanbul, 34134 Turkiye.

³ Yeditepe University, Vocational School, Mechatronic Department, 34755, Istanbul, Turkiye.

⁴ Istanbul Kultur University, Faculty of Science and Letters, Department of Physics, Istanbul, 34156 Turkiye.

* Corresponding author, e-mail: demet.demirag@yeditepe.edu.tr

Submission Date: 23.06.2022

Acceptation Date: 29.11.2022

Abstract - Ruxolitinib ($C_{17}H_{18}N_6$) is a Janus kinase (JAK) inhibitor that inhibits JAK1, JAK2, and JAK3 and with its tyrosine kinase inhibitor function It is the first drug approved for use in the treatment of myelofibrosis. The possible conformations of the ruxolitinib molecule were searched using PM3 technique and the Spartan06 software. The estimated molecular energies of the Ruxolitinib conformers, obtained by the variations in dihedral angles, were compared, and the most stable conformer was determined. To enlighten the inhibitory activity of Ruxolitinib against the apo (PDB ID: 6M03) and holo (PDB ID: 6LU7) forms of the main protease enzyme (M^{pro}) of COVID-19 and the SARSCoV-2 spike glycoprotein (PDB ID: 6VXX), molecular docking simulations were performed. The binding affinities and binding modes were determined. The binding free energies of ruxolitinib and 6M03, 6LU7, 6VXX targets calculated by the combination of Molecular Mechanics/Generalized Born Surface Area (MMGBSA) and Molecular Mechanics/Poisson-Boltzmann Surface Area (MM-PBSA) methods {MM/PB(GB)SA approach}, were found to be -22.24, -19.96 and -22.44 kcal/mol, respectively.

Keywords: Ruxolitinib, SARSCoV-2, tyrosine kinase, molecular docking

1. Introduction

Human coronaviruses, known as CoV, are enveloped positive-stranded RNA viruses belonging to the Nidovirales family. It is mostly responsible for upper respiratory and digestive tract infections [1]. SARS-CoV-2 is made up of four primary structural proteins: spike (S) glycoprotein, small envelope (E) glycoprotein, membrane (M) glycoprotein, and nucleocapsid (N) glycoprotein, as well as various auxiliary proteins. The spike, also known as S glycoprotein, is a transmembrane protein located in the virus's outer surface. There are several variants of the coronavirus, and like the other variant, the SARS-CoV-2 genome encodes spike (S) glycoproteins that protrude from the surface of mature virions. These spike glycoproteins are actively involved in the fusion of the virus, its entry into the host cell and its attachment. Its surface location is the reason why spike glycoproteins are the main target for neutralizing antibodies and host immune responses [2]. Apart from these properties, the Spike protein is also the first target for vaccine design, as we can show its central roles in viral infection and eliciting protective humoral and cell-mediated immune responses in hosts during infection [2-4]. Spike protein helps envelope viruses bind to host cells in the lower respiratory tract by forming homotrimers that protrude from the viral surface. It also shares common structural, topological, and mechanical properties with other class I fusion proteins, including the SARS-CoV-2 Spike glycoprotein, HIV envelope (Env) glycoprotein, and influenza virus hemagglutinin (HA) [5, 6].

The Ruxolitinib molecule ($C_{17}H_{18}N_6$) is one of the few hemato-oncology drugs that works by affecting epigenetic mechanisms. Ruxolitinib, which was marketed under the name Jakafi in 2011, is the first chemical agent approved for the treatment of myelofibrosis [7]. Ruxolitinib shows its

¹ Corresponding author: E-mail: demet.demirag@yeditepe.edu.tr

effectiveness by preventing the function of molecules called JAK1 and JAK2 (janus kinase), which are effective in blood cell production and immune response, that is, it has immunosuppressive properties. Ruxolitinib (INCB018424) is a potent, optional JAK1 and JAK2 inhibitor. Its main effect is inhibition of cell division and induction of apoptosis by preventing JAK from being able to phosphorylate STAT [8].

Cytoplasmic Janus protein tyrosine kinases (JAKs) are important components of various signal transduction pathways that govern cellular survival, proliferation, differentiation and apoptosis. The primary functional feature of JAK kinases is phosphorylation of cytokine and growth factor receptors. Over activation of JAK kinases has been associated with tumorigenesis. As opposed to, loss of JAK kinase function, on the other hand, has been linked to diseases such as severe combined immunodeficiency [9].

Patients with severe COVID-19 experience elevated plasma levels of proinflammatory cytokines that can cause a cytokine storm, followed by extensive immune cell infiltration into the lungs, causing alveolar damage, decreased lung function, and rapid progression to death. In addition, ruxolitinib, a powerful and optional JAK1 and JAK2 inhibitor, has started to take its place as a current issue in the treatment of diseases associated with chemokines and cytokines. As most of the upregulated cytokines signal via Janus kinase (JAK)1/JAK2, inhibition of these pathways by ruxolitinib has the potential to attenuate the COVID-19-associated cytokine storm and reduce mortality [9,10].

Yeleswaram et al. [11] investigated the effect of Ruxolitinib on the inhibition of cytokine signaling. In this study, Ruxolitinib has been shown to reduce cytokine levels and improve outcomes and reported that the patients who were given Ruxolitinib showed a numerically faster recovery from COVID-19 [11].

M^{pro} major protease inhibits the cleavage of viral polyproteins and inhibits the spread of infection. Therefore, it is a potential protein target [12-14].

To explore the usage of the Ruxolitinib in the treatment of COVID-19 and to enlighten its interaction mechanism with apo and holo forms of SARSCoV-2 main protease enzyme (M^{pro}) and with SARSCoV-2 spike glycoprotein, molecular docking simulations were performed. The binding affinities and binding modes were determined.

2. Materials and Calculations

Molecular modeling was carried out using the Spartan06 software [15] and the PM3 method [16-19]. The CAVER software [20] was used to identify potential binding sites on the receptor's surface. On the identified active sites, Molecular Docking investigations were done by using AutoDock-Vina software [21].

3. Results and Discussions

3.1. Structure

Table 1 shows the relative energies of the obtained three possible conformers of Ruxolitinib by conformational analysis and **Figure 1** shows the molecular models these conformers.

Table 1. The relative energies of three lowest energy conformers of Ruxolitinib, obtained by conformational analysis.

Conformers	Relative energy (kJ/mol)
Conformer I	0
Conformer II	0.44
Conformer III	2.48

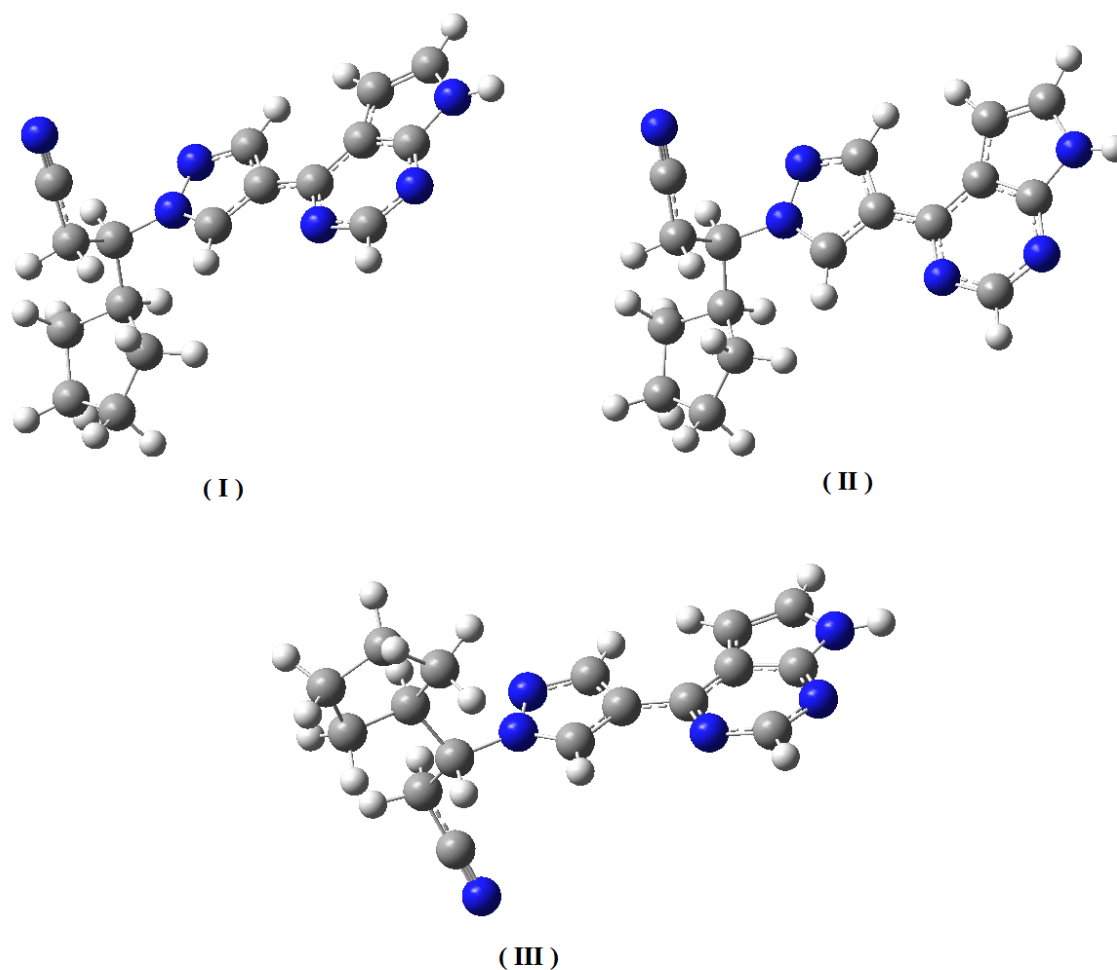


Figure 1. The three lowest energy conformers of the Ruxolitinib, obtained by conformational analysis.

3.2. Molecular Docking

To demonstrate the antiproliferative effects of ruxolitinib in our current study, molecular docking simulations were performed with the most stable structure of Ruxolitinib obtained, with SARSCoV-2 main protease enzyme (Mpro) apo/holo forms and then with SARSCoV-2 spike glycoprotein, and binding affinities and binding modes were determined.

The spike glycoprotein crystal structure (PDB ID: 6VXX), the apo form of Mpro (PDB ID: 6M03), and the holo form of Mpro (PDB ID: 6LU7) were all retrieved from the protein database [22-24], and AutoDockVina was used to perform docking tests with Ruxolitinib. Ruxolitinib's most active site was identified, and docking simulations with the apo/holo forms of the SARSCoV-2 major protease enzyme (Mpro) and the SARSCoV-2 spike glycoprotein revealed and depicted in three dimensions in Figure 2. And Ruxolitinib interactions with three receptors are shown in Figures 2-4.

The interactions between the apo form of Mpro and Ruxolitinib (shown in Figure 2) are as follows:

3.46 Å length carbon hydrogen bond between ruxolitinib and His41; 2.31 Å long hydrogen bond with Cys44; 5.12 Å long pi-alkyl interaction with Met49.

And also, 2.42 Å long hydrogen bond with Gly143, as well as 5.2 Å long pi-alkyl interaction with Cys145 and 2.21 Å long hydrogen bond with Glu166 are formed. -7.5 kcal/mol was determined as the binding affinity.

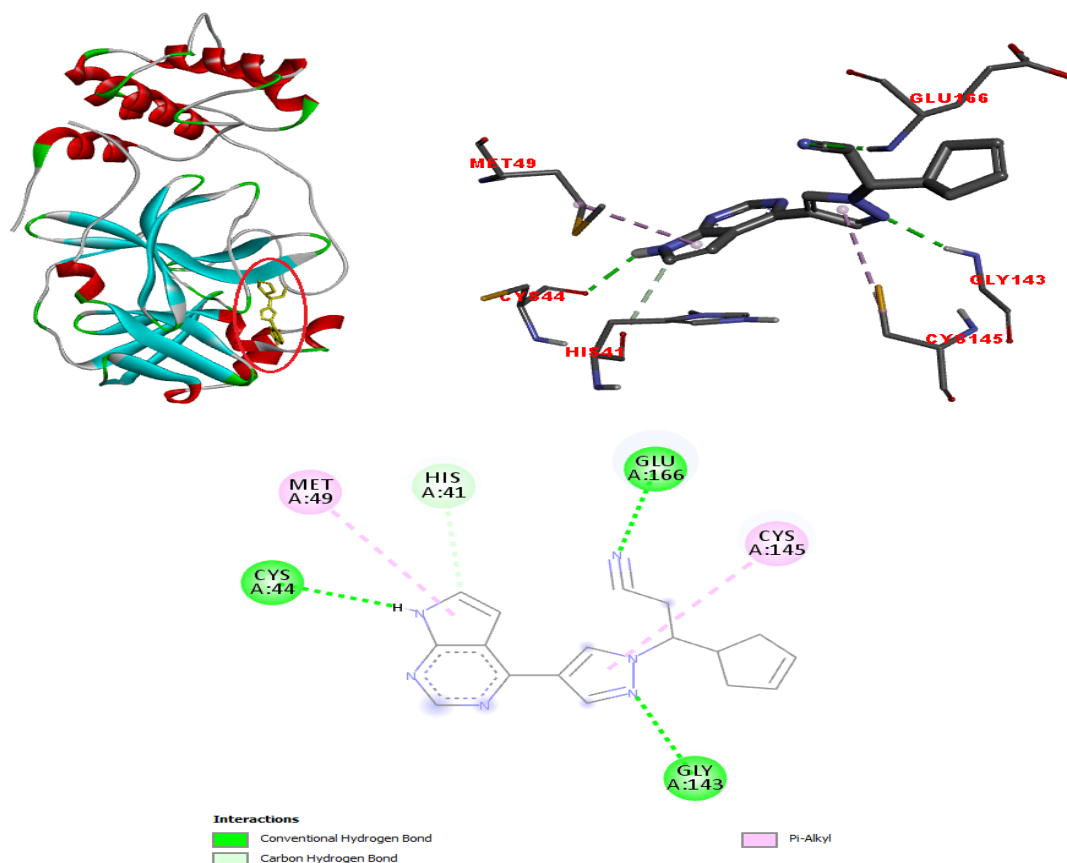


Figure 2. The 3D docked representations of the most stable conformer of Ruxolitinib in the active site of **apo** form of main protease enzyme (M^{pro}) ($\Delta G = -7.5$ kcal/mol).

Sagaama et al. [25] performed molecular docking simulation of Succinic acid (SA) with 6m03 and found that SA interacted with Ser144, Cys145, and Glu166 through hydrogen bonding interactions. This result is consistent with our findings.

Figure 3 depicts the interactions between Ruxolitinib and the active site of the **holo** version of M^{pro} in 3D docking representations. The binding affinity of Ruxolitinib docked with the holo form of SARSCoV-2 main protease enzyme (M^{pro}) is found to be -7.2 kcal/mol.

Between the ruxolitinib molecule and Val104, 5.17 Å long pi-alkyl, with Ile106, 5.37 Å long pi-alkyl; 2.64 Å long pi-donor hydrogen bond with Gln110; It was found also that with Thr292, 2.05 Å long hydrogen bond and with Phe294, 4.09 Å long pi-alkyl interaction.

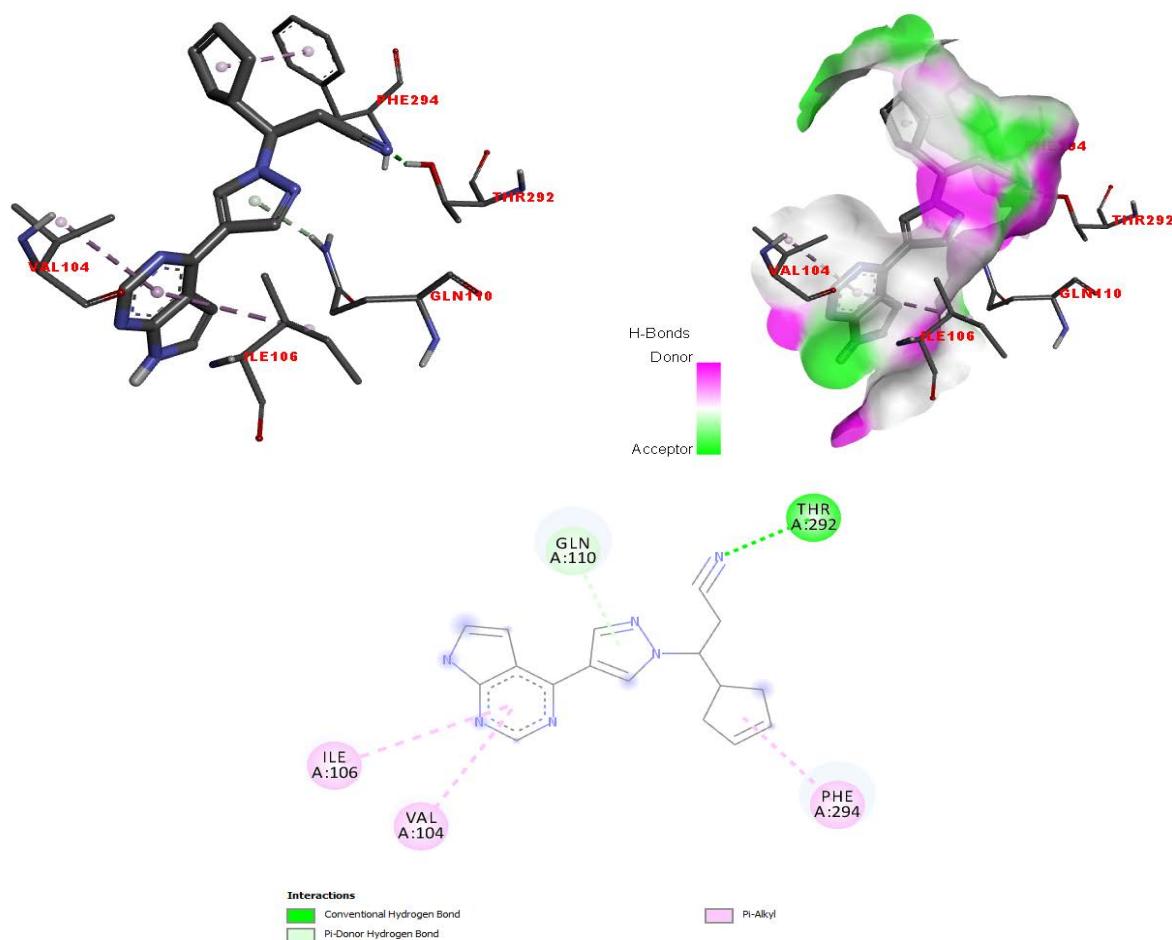


Figure 3. The most stable conformer of Ruxolitinib in the active site of **holo** form of COVID-19's main protease enzyme (Mpro) (-7.2 kcal/mol) in 3D docked representations.

Beura and Chetti [26] investigated the interactions of Chloroquine and its derivatives with SARS-CoV-2, by molecular docking simulations. In this study, it was reported that Chloroquine derivatives (CQD15 and CQD16) formed hydrogen bonds with Gln110, Thr-111, and Asp-153 as well as a pi-pi interaction with Phe8 [26]. The results are in accord with our findings.

The docking simulations of Ruxolitinib with SARSCoV-2 spike glycoprotein revealed the binding affinity as -7.5 kcal/mol. As seen in **Figure 4**, the interactions of ruxolitinib molecule with SARSCoV-2 spike glycoprotein are as follows:

5.2 Å long pi-alkyl interaction with Trp104; alkyl interaction with Ile119 (4.12 Å); hydrogen bonding interaction with Asn121 (2.68 Å); Pi-alkyl interactions (4.55 and 4.81 Å) and pi-sigma interaction (3.92 Å) with Val126; pi-donor hydrogen bond interaction with Ser172 (2.98 Å); Hydrogen bonding with Arg190 (2.57 Å); and alkyl interaction with Ile203 (4.71 Å).

Veerasamy et al. [27] investigated the potential of andrographolide derivatives against COVID-19, and molecular docking simulation of the andrographolide derivative compound 15 into 6vxx target revealed hydrophobic interactions with Val126, Leu226 and Val227 and hydrogen bonds with Asn121 and Arg190 [27].

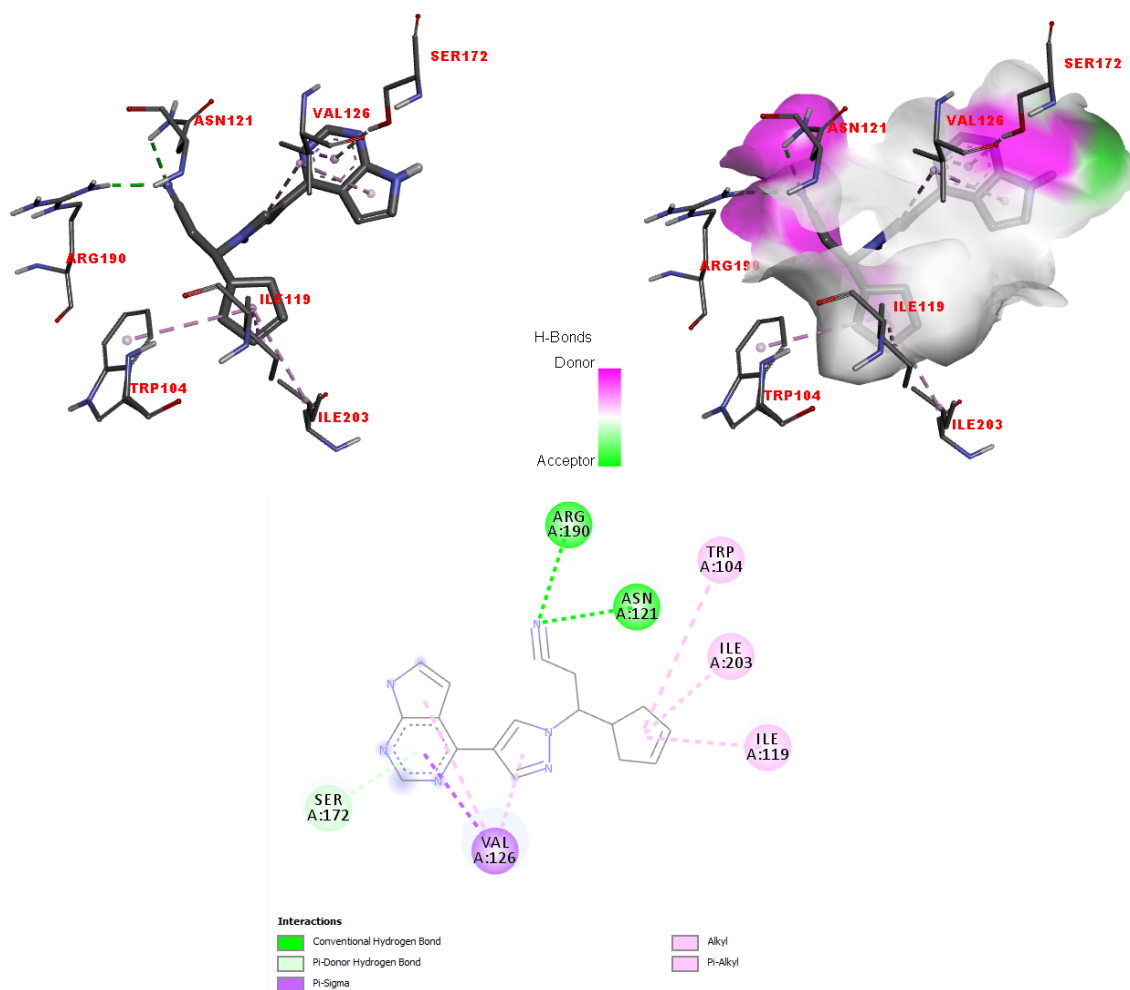


Figure 4. The most stable conformer of Ruxolitinib in the active site of the SARSCoV-2 spike glycoprotein (-7.5 kcal/mol) in 3D docked views.

In this study binding free energy of the most stable ligand protein complexes, that were identified by molecular docking studies, were also calculated. The MM/PBSA and MM/GBSA (molecular mechanical energies combined with Poisson-Boltzmann or generalized Born and surface area continuous solutions) methods estimate the free energy of binding small ligands to biological macromolecules [28-33]. By utilizing the MM/PB(GB)SA methods with the GAFF2 and ff14SB force field combination and the GB6 process, the predicted binding free energies of the ruxolitinib-Apo form, ruxolitinib-Holo form, and ruxolitinib-spike glycoprotein were -22.24, -19.96, and -22.44 kcal/mol, respectively.

4. Conclusions

Molecular docking has become an increasingly important tool for drug discovery. All docking approaches have the same goal: to anticipate the structure of the resultant complex and the biological activity of a given ligand. In this study, we present a brief introduction to evaluate Ruxolitinib's inhibitory action, the first step was to do a conformational analysis with PM3 to find the most stable conformer, and followed by docking simulations with both the apo/holo forms of M^{Pro} and spike glycoprotein. One goal of this work is to estimate the absolute binding affinity for protein-ligand complexes and the accuracy of identifying the correct binding positions generated from molecular docking programs. In this case, Ruxolitinib was shown to have the most stable structures, with binding affinities of -7.5, -7.2, and -7.5 kcal/mol with the apo/holo forms of the main protease enzyme (M^{Pro}) and spike glycoprotein, respectively. In pharmaceutical chemistry, the study of binding

affinities is of great interest, and the discovery of a novel drug often involves the synthesis and testing of hundreds of drug candidates. Naturally, it would be beneficial if computational approaches could determine binding affinities quickly and reliably.

Peer-review: Externally peer - reviewed.

Author contributions: Concept, Data Collection &/or Processing, Literature Search, Writing: A.D.D., S. C., S. A., A. E. O., S. A..

Conflict of Interest: No conflict of interest was declared by the authors.

Financial Disclosure: The authors declared that this study has received no financial support.



References

1. De Wit, E., Van Doremalen, N., Falzarano, D., & Munster, V. J. (2016). SARS and MERS: recent insights into emerging coronaviruses. *Nature Reviews Microbiology*, 14(8), 523-534.
2. Laporte, M., Raeymaekers, V., Van Berwaer, R., Vandeput, J., Marchand-Casas, I., Thibaut, H. J., ... & Stevaert, A. (2021). The SARS-CoV-2 and other human coronavirus spike proteins are fine-tuned towards temperature and proteases of the human airways. *PLoS pathogens*, 17(4), e1009500.
3. Pillaiyar, T., Meenakshisundaram, S., & Manickam, M. (2020). Recent discovery and development of inhibitors targeting coronaviruses. *Drug discovery today*, 25(4), 668-688.
4. Johnson, M. C., Lyddon, T. D., Suarez, R., Salcedo, B., LePique, M., Graham, M., ... & Ritter, D. G. (2020). Optimized pseudotyping conditions for the SARS-COV-2 spike glycoprotein. *Journal of virology*, 94(21), e01062-20.
5. Pancera, M., Zhou, T., Druz, A., Georgiev, I. S., Soto, C., Gorman, J., ... & Kwong, P. D. (2014). Structure and immune recognition of trimeric pre-fusion HIV-1 Env. *Nature*, 514(7523), 455-461.
6. Rey, F. A., & Lok, S. M. (2018). Common features of enveloped viruses and implications for immunogen design for next-generation vaccines. *Cell*, 172(6), 1319-1334.
7. Bağca, B. G., & AVCI, Ç. B. Ruxolitinib ve etki mekanizmaları. *İstanbul Bilim Üniversitesi Florence Nightingale Tıp Dergisi*, 2(2), 153-157.
8. Harrison, C., & Vannucchi, A. M. (2012). Ruxolitinib: a potent and selective Janus kinase 1 and 2 inhibitor in patients with myelofibrosis. An update for clinicians. *Therapeutic advances in hematology*, 3(6), 341-354.
9. Rane, S. G., & Reddy, E. P. (2000). Janus kinases: components of multiple signaling pathways. *Oncogene*, 19(49), 5662-5679.
10. Cao, Y., Wei, J., Zou, L., Jiang, T., Wang, G., Chen, L., ... & Zhou, J. (2020). Ruxolitinib in treatment of severe coronavirus disease 2019 (COVID-19): A multicenter, single-blind, randomized controlled trial. *Journal of Allergy and Clinical Immunology*, 146(1), 137-146.
11. Yeleswaram, S., Smith, P., Burn, T., Covington, M., Juvekar, A., Li, Y., ... & Langmuir, P. (2020). Inhibition of cytokine signaling by ruxolitinib and implications for COVID-19 treatment. *Clinical Immunology*, 218, 108517.
12. Antonopoulou, I., Sapountzaki, E., Rova, U., & Christakopoulos, P. (2022). Inhibition of the main protease of SARS-CoV-2 (Mpro) by repurposing/designing drug-like substances and utilizing nature's toolbox of bioactive compounds. *Computational and Structural Biotechnology Journal*, 20, 1306-1344.

13. Khaerunnisa, S., Kurniawan, H., Awaluddin, R., Suhartati, S., & Soetjipto, S. (2020). Potential inhibitor of COVID-19 main protease (Mpro) from several medicinal plant compounds by molecular docking study. Preprints, 2020, 2020030226.
14. Sanders, J. M., Monogue, M. L., Jodlowski, T. Z., & Cutrell, J. B. (2020). Pharmacologic treatments for coronavirus disease 2019 (COVID-19): a review. *Jama*, 323(18), 1824-1836.
15. Shao, Y., Molnar, L. F., Jung, Y., Kussmann, J., Ochsenfeld, C., Brown, S. T., ... & DiStasio Jr, R. A. (2006). Advances in methods and algorithms in a modern quantum chemistry program package. *Physical Chemistry Chemical Physics*, 8(27), 3172-3191.
16. Stewart, J.J.P. 1989. Optimization of parameters for semiempirical methods I. *Method. J. Comput. Chem.*, 10(2), 209-220.
17. Stewart, J.J.P. 1989. Optimization of parameters for semiempirical methods II. Applications. *J. Comput. Chem.*, 10 (2): 221-264.
18. Stewart, J.J.P. 1991. Optimization of parameters for semiempirical methods. III Extension of PM3 to Be, Mg, Zn, Ga, Ge, As, Se, Cd, In, Sn, Sb, Te, Hg, Tl, Pb, and Bi. *Journal of Computational Chemistry*. 12 (3), 320-341.
19. Stewart, J.J.P. 2004. Optimization of parameters for semiempirical methods IV: Extension of MNDO, AM1, and PM3 to more main group elements. *Journal of Molecular Modeling*, 10 (2), 155-64.
20. Jurcik, A.; Bednar, D.; Byska, J.; Marques, S.M.; Furmanova, K.; Daniel, L.;... Pavelka, A. CAVER Analyst 2.0: analysis and visualization of channels and tunnels in protein structures and molecular dynamics trajectories. *Bioinformatics* 2018, 34, 3586-3588.
21. Trott, O.; Olson, A.J. AutoDock Vina: Improving the speed and accuracy of docking with a new scoring function, efficient optimization, and multithreading. *J. Comput. Chem.* 2010, 31, 455-461.
22. Zhang, B.; Zhao, Y.; Jin, Z.; Liu, X.; Yang, H.; Rao, Z. The crystal structure of COVID-19 main protease in apo form. Published Online 2020. DOI: 10.2210/pdb6M03/pdb.
23. Jin, Z.; Du, X.; Xu, Y.; Deng, Y.; Liu, M.; Zhao, Y.; Zhang, B.; Li, X.; Zhang, L.; Peng, C.; Duan, Y.; Yu, J.; Wang, L.; Yang, K.; Liu, F.; Jiang, R.; Yang, X.; You, T.; Liu, X.; Yang, X.; Bai, F.; Liu, H.; Liu, X.; Guddat, L.W.; Xu, W.; Xiao, G.; Qin, C.; Shi, Z.; Jiang, H.; Rao, Z.; Yang, H. Structure of mpro from SARS-CoV-2 and discovery of its inhibitors. *Nature* 2020, 582, 289-293.
24. Walls, A. C.; Park, Y. J.; Tortorici, M. A.; Wall, A.; McGuire, A. T.; Velesler, D. Structure, function, and antigenicity of the SARS-CoV-2 spike glycoprotein. *Cell* 2020, 181(2), 281-292.
25. Sagaama, A.; Brandan, S. A.; Issa, T. B.; Issaoui, N. Searching potential antiviral candidates for the treatment of the 2019 novel coronavirus based on DFT calculations and molecular docking. *Heliyon* 2020, 6(8), e04640.
26. Beura, S.; Chetti, P. In-silico strategies for probing chloroquine based inhibitors against SARS-CoV-2. *Journal of Biomolecular Structure and Dynamics* 2021, 39(10), 3747-3759.
27. Veerasamy, R.; Karunakaran, R. Molecular docking unveils the potential of andrographolide derivatives against COVID-19: an in silico approach. *Journal of Genetic Engineering and Biotechnology* 2022, 20(1), 1-16.
28. Wang, Z.; Wang, X.; Li, Y.; Lei, T.; Wang, E.; Li, D.; Kang, Y.; Zhu, F.; Hou, T. farPPI: A web server for accurate prediction of protein-ligand binding structures for small-molecule PPI inhibitors by MM/PB (GB) SA methods. *Bioinformatics* 2019, 35, 1777-1779.
29. Hao, G.F.; Jiang, W.; Ye, Y.N.; Wu, F.X.; Zhu, X.L.; Guo, F.B.; Yang, G.F. ACFIS: A web server for fragment-based drug discovery. *Nucl. Acids Res.* 2016, 44, W550-W556.

30. Hao, G.F.; Wang, F.; Li, H.; Zhu, X.L.; Yang, W.C.; Huang, L.S.; Wu, J.; Berry, E.A.; Yang, G.F. Computational discovery of picomolar Qo site inhibitors of cytochrome bc1 complex. *J. Am. Chem. Soc.* 2012, 134, 11168-11176.
31. Yang, J.F.; Wang, F.; Jiang, W.; Zhou, G.Y.; Li, C.Z.; Zhu, X.L.; Hao, G.; Yang, G.F. PADFrag: A database built for the exploration of bioactive fragment space for drug discovery. *J. Chem. Inf. Model.* 2018, 58, 1725-1730.
32. Cheron, N.; Jasty, N.; Shakhnovich, E.I. OpenGrowth: An automated and rational algorithm for finding new protein ligands. *J. Med. Chem.* 2016, 59, 4171-4188.
33. Wang, E.; Sun, H.; Wang, J.; Wang, Z.; Liu, H.; Zhang, J.Z.H.; Hou, T. End-point binding free energy calculation with MM/PBSA and MM/GBSA: Strategies and applications in drug design. *Chem. Rev.* 2019, 119, 9478–9508.

Investigation of the Effect of Redox Mediator on the Decolorization of Anthraquinone and Diazo Dyes Using Peroxidase Enzyme

*¹ Mithat Çelebi , ² Melda Altıkatoğlu 

¹ Yalova University, Polymer Materials Engineering Depart., Faculty of Engineering, Yalova, Türkiye.

² Yıldız Technical University, Chemistry Depart. Faculty of Arts and Sciences, İstanbul, Türkiye.

* Corresponding author, e-mail: mithat.celebi@yalova.edu.tr, <https://orcid.org/0000-0002-2013-5354>.

Submission Date: 21.09.2023

Acceptation Date: 05.11.2023

Abstract

Enzymatic methods for dyestuff decolorization have many advantages compared to traditional methods. Laccase and Horseradish peroxidase enzymes are commonly utilized in enzymatic dye decolorization investigations. However, the fact that there are few dye removal experiments using lignin peroxidase enzyme. In this study, the Lignin Peroxidase enzyme was used to decolorization of Naphthol Blue Black (NBB) and Remazol Brilliant Blue R (RBBR) dyestuffs at pH 5.0 and 30 °C. In addition, the effect of 1-hydroxybenzotriazole (HOBt), as a redox mediator, on dye removal at different concentrations was investigated. The decolorization percentage of RBBR increased from 10% to 26% with the addition of a redox mediator to LiP enzyme after 24 hours. The decolorization percentage of NBB dye increased from 5% to 89% after adding HOBt to the LiP enzyme after 24 hours.

Keywords: Lignin Peroxidase, 1-hydroxybenzotriazole (HOBt), decolorization, o-dianisidine, dyestuff

Peroksidaz Enzimi ile Asidik ve Reaktif Boyarmaddelerin Rensizleştirilmesinde Redoks Mediatörün Etkisinin Araştırılması

Öz

Boyar madde renk gideriminde enzimatik yöntemler geleneksel yöntemlere göre birçok avantajları nedeni ile tercih edilmektedirler. Lakkaz ve Horseradish Peroksidaz enzimleri boyar madde giderme çalışmalarında sıklıkla kullanılmaktadır. Bu çalışmada, Lignin Peroksidaz enzimi, pH:5.0 ve 30 °C'de Naftol Blue Black ((NBB) ve Remazol Brilliant Blue R (RBBR) boyarmaddelerinin renginin giderilmesinde kullanıldı. Ayrıca, bir redoks mediatörü olan 1-hidroksibenzotriazol (HOBt)'ün farklı konsantrasyonlarda boyaların giderilmesine etkisi incelendi. LiP enzimine bir redoks mediatörü eklendiğinde, RBBR boyasının renk giderme yüzdesi 24 saatin sonunda %10'dan %26'ya yükseldi. HOBt'nin LiP enzimine eklenmesinden sonraki ilk günde, NBB boyasının renk giderme yüzdesi %5'ten %89'a yükseldi.

Anahtar kelimeler: Lignin Peoksidaz, 1-hidroksibenzotriazol (HOBt), renk giderme, o-dianisidine, boyar madde

1. Introduction

The contamination of water caused by the release of colored effluents from textile dyeing factories is one of today's major environmental issues[1]. Dyeing is widely used in plastic, paper, leather, and textile industries. Due to their widespread use in textiles, reactive dyes provide the biggest issue because they are nonbiodegradable and require considerable processing to completely remove color from wastewater[2]. Remazol Brilliant Blue R (RBBR), an anthraquinone derivative with azo, anthrazine, naphthalene, and sulfonated groups in its structure, is an important class of largely hazardous and resistant organic pollutants (see Fig. 1a)[3]. Naphthol Blue Black (NBB) is composed of azo, phenolic, aniline, naphthalene, and sulfonated structures (see Fig. 1b). It is a commercially important acidic diazo dye with strong photo- and thermal endurance[1]. These environmental pollutants could be removed by using physical, chemical, and biological techniques[4].

Polymers are frequently utilized in the chemical industry due to their lightweight, low cost, and ease of molding [5] as automotive parts, building materials, household appliances, electronic

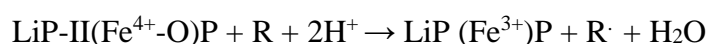
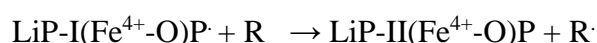
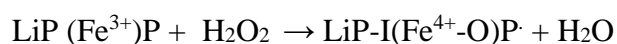
materials [6], and wastewater treatment [7]. Lignin is a complex aromatic polymer that is the second most important sustainable carbon source on the planet after cellulose, and it contains around 30% non-fossil biological carbon. The most significant challenge to utilizing renewable resources is lignin degradation. Enzymes are a specific instance of a biological approach. Enzymes such as lignin peroxidase (LiP) are investigated in dye decolorization. The possible usage of lignin-degrading bacteria and lignin peroxidase has gained interest as they can provide environmentally benign ways for the treatment of dye-containing effluent from different sectors [8], [9].

Proteins are a type of biodegradable polymer derived from biomass [10]. Enzymes are protein-structured biological catalysts [11]. Wastewater treatment with enzymes and nanoparticles has been discovered to be very successful and less harmful since enzyme has a wide range of uses such as catalytic conversion, biological remediation, and biosensors [12]. Although the use of enzymes in wastewater treatment was initially advocated in the 1930s, the concept of environmental biocatalysis, which is the use of enzymes to eliminate and degradation of target contaminants, became apparent in the 1970s [13]. Enzymes can degrade pollutants by increasing their water dissolution, allowing for additional degradation by microorganisms, or by promoting insolubility and later removal from the waste from the industry system [13], [14]. In recent years, researchers have used a variety of enzymes to remove colors from wastewater, including Horseradish Peroxidase [15]–[18], Lignin Peroxidase [9], [19]–[21], Manganese Peroxidase [22], [23], Soybean Peroxidase [24], and laccase [25].

Peroxidases (EC 1.11.1.x) are chemically composed proteins (metalloproteins) that catalyze the oxidation of a variety of substrates by using hydrogen peroxide or other organic peroxides as electron acceptors [26]. Most peroxidases are glycoproteins with N-linked oligosaccharides. These enzymes can be found in practically every field in nature and perform a variety of physiological activities. The most well-known peroxidase enzymes include chloro peroxidase (CPO) from *Caldariomyces fumago*, lignin peroxidase (LiP) from *Phanerochaete chrysosporium*, manganese peroxidase (MnP), and horseradish peroxidase (HRP) from *Coriopsis gallica*. To remove dyes, lignin peroxidase, manganese peroxidase, soybean peroxidase, horseradish peroxidase (HRP), and laccase enzymes are utilized [15], [27], [28].

Lignin peroxidases (EC 1.11.1.14) are glycolysis enzymes with a molecular weight range from 38 to 43 kDa, acidic isoelectric points, and pH values as low as 3.3–4.7. In their active areas, proteins and protoporphyrin IX coexist. LiP acts as a conventional peroxidase, being oxidized by H₂O₂ to the two electron-deficient Compound I. Compound II was the portion that lacked an electron. While most peroxidases exclusively oxidize phenols and aromatic amines, LiPs also oxidize non-phenolic molecules [29], [30]. In lignin structures, LiP-catalyzed oxidation removes one electron from the aromatic ring to generate an aryl cation radical. Different products are generated in the presence of molecular oxygen [31].

LiP catalyzes H₂O₂-dependent oxidation in various lignin model compounds via the chemical sequence outlined below.



P: is pofrin, R: is an aromatic substrate such as veratryl alcohol. LiP Compound I (LiP-I) has two equivalent structures, one of which is the oxyferyl point, which is oxidized to H₂O₂, and the other is the deporphyrin (pi) cation radical. In contrast, LiP compound II can only have one oxidized equivalent structure. Compound I is formed by oxidizing Substrate R. LiP is catalytically transformed into the inactive intermediate Compound III in the presence of high H₂O₂. Native LiP can be

regenerated by spontaneous dissociation from Compound III, which results in the release of superoxide[32]. In general, LiP catalyzes the breakage of C_{alpha}-C_{beta} bonds in the model compound's propyl chain [31].

Redox mediators, initially identified by Bourbonnais and Paice (1990), allow laccases to oxidize nonphenolic substances, thus increasing the substrate range that these enzymes may oxidize[33]. Once substrates are too large to enter the enzyme's active site, mediators, which are tiny molecules, are required. A mediator is a type of molecule that serves as an electron transporter. When the enzyme oxidizes it, a very powerfully oxidizing intermediate chemical is generated. When passed through the enzymatic package, it can quickly oxidize any substrate [34]. As dyes are unstable and complex, they are difficult to remove using traditional water treatment methods. Enzymatic catalysis with redox aids is widely used in the degradation of polycyclic compounds, phenols, aromatic amines, biphenyls, pesticides, insecticides, and other organic molecules. Bromophenol, 2,4-dichlorophenol, guaiacol, 1-hydroxybenzotriazole (HOBt), m-cresol, quinol, syringaldehyde, vanillin, and violuric acid are the most important of these [35], [36].

2,2'-azino-bis(3-ethylbenzothiazoline)-6-sulfonate (ABTS) and HOBt are the synthetic mediators that are most frequently utilized to improve the oxidation of organic contaminants[33]. Nguyen et. al. investigated the effect of a redox mediator, syringaldehyde, on the degradation of organic pollutants in an enzymatic membrane reactor and concluded that the redox mediator considerably enhanced the degradation of organic pollutants and the toxicity of wastewater[37]. Hirai investigated the role of 1-hydroxybenzotriazole (HOBt) in the oxidation of Guaiacol by laccase from *Trametes versicolor*[38]. Goodwin et. al. investigated the veratryl alcohol (VA)-mediated oxidation of chlorpromazine (CPZ) by using lignin peroxidase (LiP). They concluded that chlorpromazine was a suitable substrate for the LiP enzyme. Also, they demonstrated how the CPZ oxidation kinetics in the presence of VA could operate as a redox mediator for oxidation processes catalyzed by LiP[39]. Jamal et. al. used 9 different redox mediators (HOBt, Syringaldehyde, Guaiacol, Vanillin, Bromophenol, 2-4, Dichlorophenol, Violuric acid, Quinol and m-Cresol) in addition to the peroxidase enzyme in the removal of disperse dyes, and the highest dye removal results were achieved with HOBt-mediated oxidation of the dyes[35]. Matto and Husain removed the direct dyes by turnip peroxidase enzyme using redox mediators such as HOBt ve Violuric acid. They achieved the highest dye removal values at pH: 5.0 and 30 °C[40]. In this study, the enzymatic approach for dye removal was preferred because it is more environmentally friendly than traditional methods. Since the lignin peroxidase enzyme was insufficient to decolorize the NBB and RBBR dyestuffs, a redox mediator was added to the Lip enzyme. According to our knowledge, this study was the first to use HOBt-mediated oxidation of NBB and RBBR dyestuffs by LiP enzyme. According to the above-mentioned research in the literature, the peroxidase enzyme achieved the highest dye removal values at pH: 5 and 30 C, hence it was studied at these optimum conditions.

2. Materials and Methods

Remazol Brilliant Blue R (RBBR), Hydrogen peroxide (H₂O₂) 30%, and Lignin Peroxidase (specific activity: >0.1 U/mg) were bought from Sigma Aldrich. Dimethyl sulfoxide (DMSO), o-dianisidine, acetic acid, 1-hydroxybenzotriazole hydrate (HOBt), and Naphthol Blue Black were received from Fluka. None of the chemicals were further purified before use. Shimadzu UV-1800 spectrophotometer was used for UV-VIS spectroscopy studies.

2.1. Peroxidase Activity

Lignin peroxidase activity is frequently assessed by oxidation of veratryl alcohol (3,4-dimethoxybenzyl alcohol) [41]. In this study, peroxidase activity was measured by monitoring the H₂O₂-mediated oxidation of o-dianisidine at 460 nm with extinction coefficients 11.300 M⁻¹ cm⁻¹ [42]. The enzyme concentration was prepared to 0.004 mg/mL. The enzymatic activity of the

Peroxidase was determined using the following steps at pH 5.0 and 30 °C. 930 µL sodium acetate buffer solution (0.05 M, pH: 5.0), 20 µL o-dianisidine (10 mM), and 40 µL LiP solution were added to a quartz cuvette and the cuvette was stirred with an orbital shaker. Finally, 10 µL H₂O₂ from 3% H₂O₂ was added to initiate the reaction and then, OD₄₆₀ of this solution was acquired at each tenth minute. The enzyme activity was calculated using Equation 1. A unit was defined as the amount of enzyme required to oxidize one µmol of substrate per minute [3], [15], [28]. A₄₆₀ is the absorbance of the solution at 460 nm, and M_ε is the molar absorption coefficient of o-dianisidine (11.300). c is Lignin Peroxidase enzyme concentration (milligrams per milliliter) referred to in equation 1 [28].

$$\frac{U}{mg} = \left(\frac{A(460) \times 10^6}{M_{\epsilon} \times C(LiP) \times t} \right) \quad (1)$$

2.2. Decolorization

Remazol Brilliant Blue R and Naphthol Blue Black dyestuffs were prepared at a concentration of 40 mg/mL. 100 mM HBT was prepared in 50% Dimethyl sulfoxide (DMSO) and 0.05 M sodium acetate buffer at pH 5.0[43]. Decolorization of RBBR and NBB was determined by measuring dye solution absorbance at 594 nm and 620 nm, respectively for 14 days at 30 °C. The glass tube was filled with 10 µL dyestuff solution, LiP enzyme (30 µL, 50 µL, and 100 µL for different reactions), and/or redox mediator (100 mM) (50 µL, 100 µL, and 150 µL HOBt) respectively. Then, the volume of the glass tube was completed to 2990 µL with sodium acetate buffer (0.05 M, pH:5.0). The decolorization reaction was then initiated with the addition of 10 µL H₂O₂ (3%). The total reaction volume was 3 mL. The concentration of both dyestuffs (RBBR and NBB) in the glass tube is 133 mg/L. The final concentration of the redox mediator was 1,66 mM, 3.32 mM, and 4.98 mM for 50 µL, 100 µL, and 150 µL pipetted respectively. Dye removal experiments were first carried out in the UV-Vis. cuvette of a temperature-controlled UV-Vis spectrophotometer. However, no decrease was observed in the UV-Vis spectra of the dyes in the measurements made at 5-10-minute intervals during the day. For this reason, experimental studies were continued by making measurements at longer intervals in closed glass tubes.

Percentages of dye decolorization values were calculated using Equation 2, where A_b is the absorbance of the dye solution before the enzyme reaction begins and A_a is the absorbance of the dye solution after the enzyme reaction begins [15]. Table 1 describes the characteristics of dyestuffs. The chemical structures of dyestuffs are illustrated in Figure 1.

$$(\%)Decolorization\ of\ Dyestuff = \frac{A_b - A_a}{A_a} \times 100 \quad (2)$$

Table 1. General characteristics of Remazol Brilliant Blue R and Naphthol Blue Black

Parameters	Remazol Brilliant Blue R	Naphthol Blue Black
Color Index (C.I)	Reactive Blue 19	Acid Black 1
Molecular Weight (M _w)	624.54 g/mol	616.49 g/mol
Maximum Absorption Wavelength (λ _{max})	594 nm	620 nm
Chemical structure	Anthraquinone	Diazo

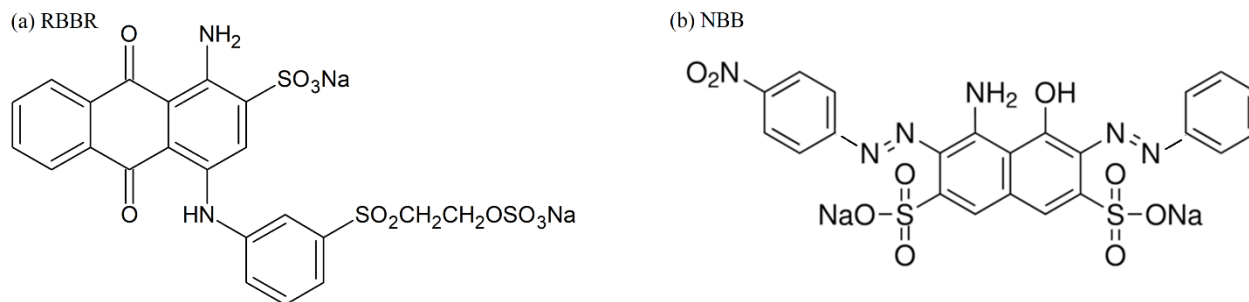


Figure 1. Molecular structure of Remazol Brilliant Blue R (RBBR) (a) and Naphthol Blue Black (NBB) (b) dyestuffs.

3. Results and Discussions

The peroxidase activity of the lignin peroxidase enzyme was calculated as 27.5 IU/mg in this study at pH 5.0 by using the o-dianisidine substrate. The Lignin Peroxidase (LiP) enzyme activity was assessed by Giap et al. using veratraldehyde substrate at pH 3.0 (0.25 M sodium tartrate) and 10 mm H₂O₂. LiP from an isolated strain of *Pleurotus pulmonarius* CPG6 was purified with a specific activity of 6.59 U/mg by Giap et al. in their research [20].

The decolorization percentage of RBBR increased from 11% to 37% with the addition of the redox mediator (100μL) to the LiP enzyme (30μL) on the 14th day, as seen in Figure 2. The decolorization percentage of RBBR On the first day, increasing the amount of redox mediator to the LiP enzyme (50μL) from 100μL to 150 μL enhanced from 38% to 73%.

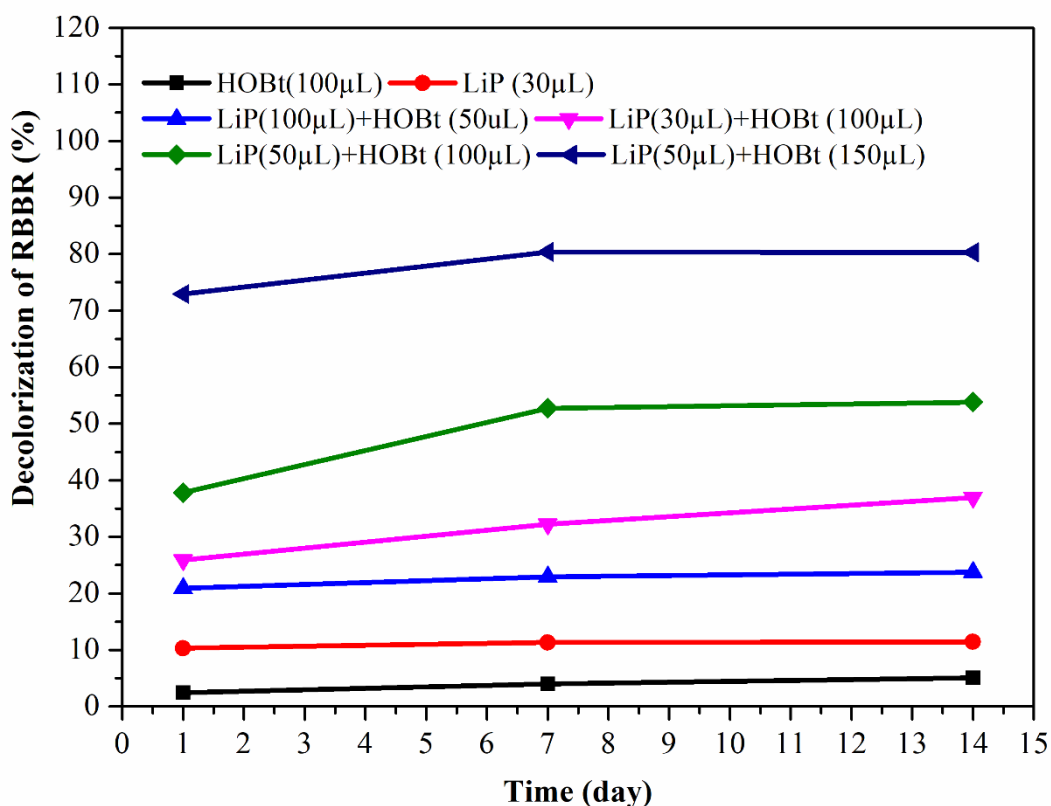


Figure 2. Decolorization of RBBR dyestuff with LiP, HOBT and LiP+HOBT at pH: 5.0 and 30 °C.

RBBR dyestuff was eliminated by 32% using LiP enzyme after 12 hours, according to Giap et. al. (2009) [20].

Figure 3 shows that when the HOBt (100 μ L) was added to the LiP enzyme (30 μ L), the percentage of NBB dye removed increased from 5% to 89% after 24 hours and from 6% to 97% after 14 days. The percentages of decolorization values were 43%, 89%, 87%, and 87% after 24 hours when the HOBt volume was kept constant at 100 μ L and the LiP enzyme was increased to 10 μ L, 30 μ L, 50 μ L, and 75 μ L, respectively. Using more than 30 μ L of LiP enzyme together with HOBt to decolorize the NBB had no significant effect on dyestuff decolorization; on the contrary, it promoted the production of additional by-products.

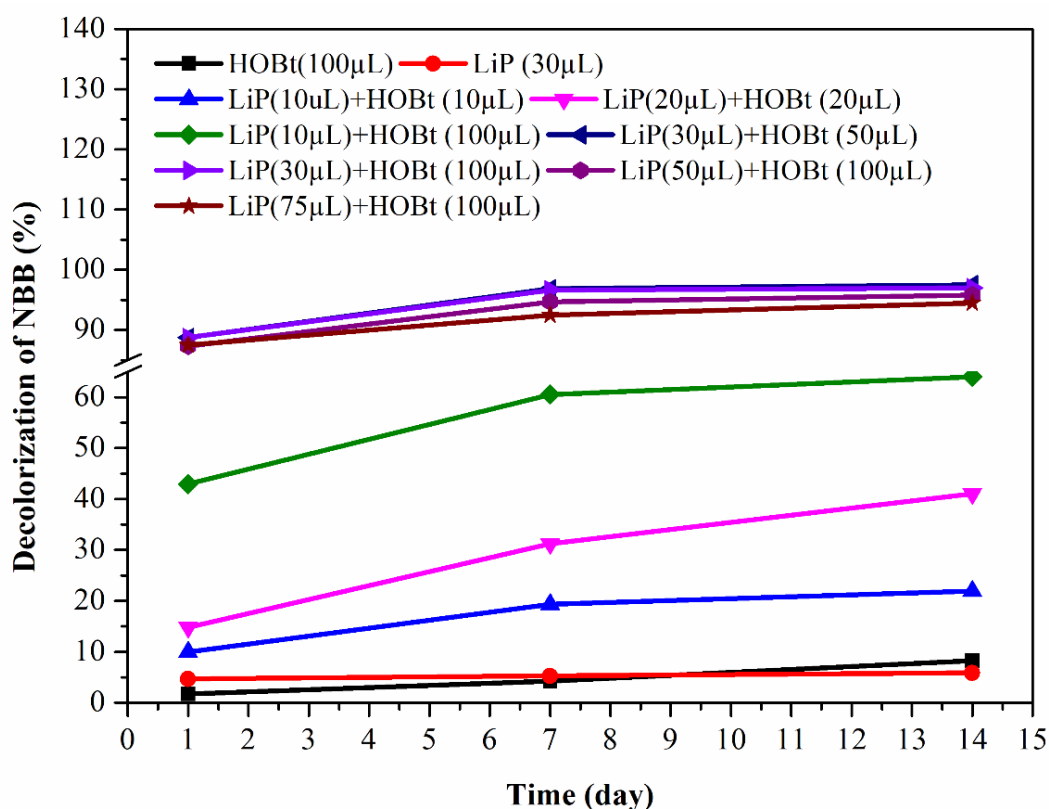


Figure 3. Decolorization of NBB dyestuff with LiP, HOBt and LiP+HOBt at pH: 5.0 and 30 $^{\circ}$ C.

Ferreira-Leitao et. al. investigated the decolorization of Methylene Blue (MB) dye with the Lignin Peroxidase enzyme from *Phanerochaete chrysosporium* at various MB: H₂O₂ molar ratios. The dye decolorization percentage of MB dye (50 mg/L) was measured to be approximately 90%, 10%, and 10% at 1:5, 1:10, and 1:20 MB: H₂O₂ molar ratios, respectively[13]. Immobilization of Ca-alginate in a packed bed reactor system, LiP was also used to decolorize the Remazol Brilliant Blue R dye by Bilal and Iqbal (2019). Bilal and Iqbal (2019) found that the ability of immobilized LiP to decolorize the RBBR in multiple batch cycles indicated its potential for bioremediation [44]. Tartarazine, an azo dye, was eliminated by 20% after 8 days with *Pleurotus sajorcaju* by Chagas et al. Their findings revealed that *P. sajorcaju* had the maximum Glucose-1-oxidase (GOD) activity on the second day of growth. The authors found that this fungus does not produce lignin peroxidase and that the initiation of degradation could be caused by free radicals produced by GOD or laccase enzymes [45].

LiP is a glycosylated enzyme that can biodegrade and biotransform highly hazardous phenolic chemicals found in bleach plant effluents. The peroxidase enzymes have been used in a variety of commercial applications, including dye decolorization, bio-delignification for biofuel production, organic pollutant bioremediation, biosensor creation, and sewage treatment [44]. Enzymatic

treatments are highly useful because enzymes operate on wastewater even when they are present in highly diluted solutions and are resistant to the action of certain bacteria involved in dye degradation. However, some resistant dyes are not decolorized in the presence of such enzymes (HRP, LiP, MnP, and laccase). Redox mediators increase the availability of substrates and improve the efficiency of difficult chemical degradation [46].

While the percentage of LiP enzyme-related dye decolorization was relatively low in this investigation, the addition of a redox mediator (HOBt) resulted in a significant rise in dye decolorization values, as shown in Figures 2 and 3. While the HRP enzyme removed over 100% of these dyes in a relatively short time at pH: 5 and 30°C [3], [47], the dyestuffs decolorization values were very low with the LiP enzyme, and the dye removal period was weeks in this study.

4. Conclusions

Dye wastewater from the textile and dyestuff industries must be treated since it causes visual pollution and poses a risk to aquatic and terrestrial life. Traditional wastewater treatment technologies are ineffective due to the properties of this wastewater. Therefore, redox-mediated enzymatic oxidation of organic compounds has been used as an environmental method. Redox-mediated decolorization of RBBR and NBB was performed by the Lignin Peroxidase enzyme at optimum conditions in this study. The decolorization percentage of RBBR was enhanced with increasing enzyme and redox mediator concentration. However, the redox mediator (HOBt) did not affect the decolorization of NBB when the LiP enzyme concentration was more than 30 µL. HOBt showed a particularly effective influence on NBB decolorization at low enzyme concentrations. It was concluded that the LiP enzyme with redox mediator decolorized the NBB dye more effectively than the RBBR dyestuff. These encouraging findings recommend the use of a redox-mediated decolorization of dyestuffs by the Lignin Peroxidase enzyme to degrade various resistant substances.

Peer-review: Externally peer-reviewed.

Author contributions: Concept – Mithat Çelebi, Melda Altıkatoğlu; Literature Search – Mithat Çelebi; Writing – Mithat Çelebi, Melda Altıkatoğlu

Conflict of Interest: No conflict of interest was declared by the authors.

Financial Disclosure: The authors declared that this study has received no financial support.

References

- [1] O. Bechiri, M. Abbessi, and M. E. H. Samar, “Decolorization of organic dye (NBB) using Fe(III)P2W12Mo5/H2O2 system,” *Desalination Water Treat*, vol. 51, no. 31–33, 2013, doi: 10.1080/19443994.2013.766648.
- [2] A. Raes *et al.*, “Adsorption Potential of Schizophyllum commune White Rot Fungus for Degradation of Reactive Dye and Condition Optimization: A Thermodynamic and Kinetic Study,” *Adsorption Science and Technology*, vol. 2023, 2023, doi: 10.1155/2023/4725710.
- [3] M. Celebi, M. Altikatoglu, Z. M. Akdeste, and H. Yildirim, “Determination of decolorization properties of Reactive Blue 19 dye using Horseradish Peroxidase enzyme,” *Turkish Journal of Biochemistry*, vol. 38, no. 2, pp. 200–206, 2013, doi: 10.5505/tjb.2013.96636.
- [4] G. Crini and E. Lichtfouse, “Green adsorbents for pollutant removal: fundamentals and design,” *Springer Nature*, 2018.
- [5] E. Akdogan, “Investigation of the Effects of Unidirectional Compression on the Hardness of High-Density Polyethylene Materials,” *Open Journal of Nano*, vol. 7, no. 2, 2022, doi: 10.56171/ojn.1110326.

- [6] M. Uluskan, “Decreasing Defects in Plastic Injection Molding and Vibration Welding Processes Through Statistical Process Control,” 2021.
- [7] R. M. El Khaldi *et al.*, “Fabrication of high-performance nanofiber-based FO membrane,” *Desalination Water Treat*, vol. 147, pp. 56–72, 2019, doi: 10.5004/dwt.2019.23699.
- [8] S. Das, A. Gole, A. Chakraborty, S. Mal, S. Rudra, and D. Ghosh, “Lignocellulolytic Microbial Systems and its Importance in Dye Decolourization: A Review,” *J Pure Appl Microbiol*, vol. 17, no. 2, 2023, doi: 10.22207/jpam.17.2.19.
- [9] W. J. Guo *et al.*, “Design and engineering of an efficient peroxidase using myoglobin for dye decolorization and lignin bioconversion,” *Int J Mol Sci*, vol. 23, no. 1, 2022, doi: 10.3390/ijms23010413.
- [10] M. Çelebi and İ. Karagöz, “Biyobozunur Polimerler Ve Özellikleri; Nişasta, Poli(Glikolik Asit), Poli(Laktik Asit) Ve Poli(ε Kaprolakton),” *Gece Akademi Yayıncılık, Mühendislik Alanında Yeni Ufuklar, Chapter 11*, pp. 249–266, 2019.
- [11] G. M. Cooper, “The Central Role of Enzymes as Biological Catalysts,” *The Cell: A Molecular Approach*, 2000.
- [12] T. Angelin Swetha, K. Mohanrasu, A. Bora, V. Ananthi, and A. Arun, “Enzymes incorporated nanotechnology for wastewater treatment,” in *Handbook of Microbial Nanotechnology*, 2022. doi: 10.1016/B978-0-12-823426-6.00021-8.
- [13] V. S. Ferreira-Leitao, M. E. A. de Carvalho, and E. P. S. Bon, “Lignin peroxidase efficiency for methylene blue decolouration: Comparison to reported methods,” *Dyes and Pigments*, vol. 74, no. 1, pp. 230–236, 2006, doi: 10.1016/j.dyepig.2006.02.002.
- [14] M. Celebi, M. Arif, M. Altikatoglu, and H. Yildirim, “Removal of cationic dye from textile industry wastewater with using enzyme , fungus and polymer,” *The Online Journal of Science and Technology*, vol. 3, no. 2, pp. 39–45, 2013, [Online]. Available: <http://www.tojsat.net/index.php/tojsat/article/view/107/111>
- [15] M. Çelebi, Z. Ö. Özdemir, and M. Topuzoğullari, “Microwave-assisted rapid conjugation of horseradish peroxidase-dextran aldehyde with Schiff base reaction and decolorization of Reactive Blue 19,” *Turk J Chem*, vol. 46, no. 3, 2022, doi: 10.55730/1300-0527.3378.
- [16] M. Altikatoglu and Y. Basaran, “Additive effect of dextrans on the stability of horseradish peroxidase,” *Protein Journal*, vol. 30, no. 2, pp. 84–90, 2011, doi: 10.1007/s10930-011-9306-4.
- [17] U. Kalsoom *et al.*, “Biocatalytic degradation of reactive blue 221 and direct blue 297 dyes by horseradish peroxidase immobilized on iron oxide nanoparticles with improved kinetic and thermodynamic characteristics,” *Chemosphere*, vol. 312, 2023, doi: 10.1016/j.chemosphere.2022.137095.
- [18] P. Xie *et al.*, “Phenoxyl mediators improve enzymatic degradation of organic pollutants: Effect and mechanism,” *Int J Biol Macromol*, vol. 215, 2022, doi: 10.1016/j.ijbiomac.2022.06.124.
- [19] R. Shaheen, M. Asgher, F. Hussain, and H. N. Bhatti, “Immobilized lignin peroxidase from *Ganoderma lucidum* IBL-05 with improved dye decolorization and cytotoxicity reduction properties,” *Int J Biol Macromol*, vol. 103, 2017, doi: 10.1016/j.ijbiomac.2017.04.040.
- [20] V. D. Giap *et al.*, “Purification and characterization of lignin peroxidase from white-rot fungi *Pleurotus pulmonarius* CPG6 and its application in decolorization of synthetic textile dyes,” *Journal of General and Applied Microbiology*, vol. 68, no. 6, 2022, doi: 10.2323/jgam.2022.05.005.
- [21] R. Ten Have, R. G. De Thouars, H. J. Swarts, and J. A. Field, “Veratryl alcohol-mediated oxidation of isoeugenyl acetate by lignin peroxidase,” *Eur J Biochem*, vol. 265, no. 3, 1999, doi: 10.1046/j.1432-1327.1999.00808.x.
- [22] H. Rezik *et al.*, “Physical and enzymatic properties of a new manganese peroxidase from the white-rot fungus *Trametes pubescens* strain i8 for lignin biodegradation and textile-dyes biodecolorization,” *Int J Biol Macromol*, vol. 125, 2019, doi: 10.1016/j.ijbiomac.2018.12.053.
- [23] Y. Chang, D. Yang, R. Li, T. Wang, and Y. Zhu, “Textile dye biodecolorization by manganese peroxidase: A review,” *Molecules*, vol. 26, no. 15, 2021. doi: 10.3390/molecules26154403.
- [24] B. M. Althahir *et al.*, “Soybean peroxidase catalyzed decoloration of acid azo dyes,” *J Health Pollut*, vol. 10, no. 25, 2020, doi: 10.5696/2156-9614-10.25.200307.
- [25] E. A. M. Ali, S. Abd Ellatif, and E. S. Abdel Razik, “Production, purification, characterization and immobilization of laccase from *Phoma betae* and its application in synthetic dyes decolorization,” *Egyptian Journal of Botany*, vol. 60, no. 1, 2020, doi: 10.21608/ejbo.2019.19226.1381.

- [26] N. Šekuljica *et al.*, “Decolorization of anthraquinonic dyes from textile effluent using horseradish peroxidase: Optimization and kinetic study,” *Scientific World Journal*, vol. 2015, 2015, doi: 10.1155/2015/371625.
- [27] M. Altikatoglu and M. Celebi, “Enhanced stability and decolorization of Coomassie Brilliant Blue R-250 by dextran aldehyde-modified horseradish peroxidase,” *Artif Cells Blood Substit Immobil Biotechnol*, vol. 39, no. 3, pp. 185–90, 2011.
- [28] M. Celebi, M. A. Kaya, M. Altikatoglu, and H. Yildirim, “Enzymatic decolorization of anthraquinone and diazo dyes using horseradish peroxidase enzyme immobilized onto various polysulfone supports,” *Appl Biochem Biotechnol*, vol. 171, no. 3, pp. 716–730, 2013.
- [29] T. K. Kirk and D. Cullen, *Enzymology and molecular genetics of wood degradation by white-rot fungi*. 1998.
- [30] P. Chowdhary, N. More, A. Yadav, and R. N. Bharagava, “Ligninolytic enzymes: An introduction and applications in the food industry,” in *Enzymes in Food Biotechnology: Production, Applications, and Future Prospects*, 2018. doi: 10.1016/B978-0-12-813280-7.00012-8.
- [31] T. K. Kirk and R. L. Farrell, “Enzymatic ‘combustion’: the microbial degradation of lignin,” *Annual review of microbiology*, vol. 41. 1987. doi: 10.1146/annurev.mi.41.100187.002341.
- [32] H. Wariishi and M. H. Gold, “Lignin peroxidase compound III. Mechanism of formation and decomposition,” *Journal of Biological Chemistry*, vol. 265, no. 4, 1990, doi: 10.1016/s0021-9258(19)39941-7.
- [33] M. Husain and Q. Husain, “Applications of redox mediators in the treatment of organic pollutants by using oxidoreductive enzymes: A review,” *Critical Reviews in Environmental Science and Technology*, vol. 38, no. 1. 2008. doi: 10.1080/10643380701501213.
- [34] O. Faix, “Book Review: Biopolymers. Biology, Chemistry, Biotechnology, Applications. Vol. 1: Lignin, Humic Substances and Coal. Edited by Alexander Steinbüchel and Martin Hofrichter,” *Angewandte Chemie International Edition*, vol. 41, no. 11, 2002, doi: 10.1002/1521-3773(20020603)41:11<1963::aid-anie1963>3.0.co;2-f.
- [35] F. Jamal, P. K. Pandey, and T. Qidwai, “Potential of peroxidase enzyme from *Trichosanthes dioica* to mediate disperse dye decolorization in conjunction with redox mediators,” *J Mol Catal B Enzym*, vol. 66, no. 1–2, pp. 177–181, 2010, doi: 10.1016/j.molcatb.2010.05.005.
- [36] Q. Husain, “Potential Applications of the Oxidoreductive Enzymes in the Decolorization and Detoxification of Textile and Other Synthetic Dyes from Polluted Water: A Review,” *Crit Rev Biotechnol*, vol. 26, no. 4, pp. 201–221, 2006, doi: 10.1080/07388550600969936.
- [37] L. N. Nguyen *et al.*, “The effects of mediator and granular activated carbon addition on degradation of trace organic contaminants by an enzymatic membrane reactor,” *Bioresour Technol*, vol. 167, 2014, doi: 10.1016/j.biortech.2014.05.125.
- [38] H. Hirai, H. Shibata, S. Kawai, and T. Nishida, “Role of 1-hydroxybenzotriazole in oxidation by laccase from *Trametes versicolor*. Kinetic analysis of the laccase-1-hydroxybenzotriazole couple,” *FEMS Microbiol Lett*, vol. 265, no. 1, 2006, doi: 10.1111/j.1574-6968.2006.00474.x.
- [39] D. C. Goodwin, S. D. Aust, and T. A. Grover, “Evidence for Veratryl Alcohol as a Redox Mediator in Lignin Peroxidase-Catalyzed Oxidation,” *Biochemistry*, vol. 34, no. 15, 1995, doi: 10.1021/bi00015a017.
- [40] M. Matto and Q. Husain, “Decolorization of direct dyes by salt fractionated turnip proteins enhanced in the presence of hydrogen peroxide and redox mediators,” *Chemosphere*, vol. 69, no. 2, 2007, doi: 10.1016/j.chemosphere.2007.03.069.
- [41] S. Hariharan and P. Nambisan, “Optimization of lignin peroxidase, manganese peroxidase, and lac production from *Ganoderma lucidum* under solid state fermentation of pineapple leaf,” *Bioresources*, vol. 8, no. 1, 2013, doi: 10.15376/biores.8.1.250-271.
- [42] E. Keyhani, J. Keyhani, S. Saeidian, F. Attar, and S. Oveissi, “Identification of enzymatic properties in *Crocus sativus* roots,” in *Acta Horticulturae*, 2007. doi: 10.17660/ActaHortic.2007.739.29.
- [43] H. Claus, G. Faber, and H. König, “Redox-mediated decolorization of synthetic dyes by fungal laccases,” *Appl Microbiol Biotechnol*, vol. 59, no. 6, 2002, doi: 10.1007/s00253-002-1047-z.
- [44] M. Bilal and H. M. N. Iqbal, “Lignin peroxidase immobilization on Ca-alginate beads and its dye degradation performance in a packed bed reactor system,” *Biocatal Agric Biotechnol*, vol. 20, 2019, doi: 10.1016/j.bcab.2019.101205.

- [45] E. P. Chagas and L. R. Durrant, “Decolorization of azo dyes by *Phanerochaete chrysosporium* and *Pleurotus sajorcaju*,” *Enzyme Microb Technol*, vol. 29, no. 8–9, 2001, doi: 10.1016/S0141-0229(01)00405-7.
- [46] F. Jamal, “Functional Suitability of Soluble Peroxidases from Easily Available Plant Sources in Decolorization of Synthetic Dyes,” in *Advances in Treating Textile Effluent*, 2011. doi: 10.5772/20370.
- [47] S. Onder, M. Celebi, M. Altikatoglu, A. Hatipoglu, and H. Kuzu, “Decolorization of naphthol blue black using the horseradish peroxidase,” *Appl Biochem Biotechnol*, vol. 163, no. 3, pp. 433–443, 2011.

Effect of Different Passivation Treatments on Alkaline Zn-Ni Coatings: Corrosion Resistance and Adhesion Performance of Geomet 321 and ML Black Coatings

*^{1,2} İbrahim USTA , ^{1,3} Oğuz YILMAZ , ^{1,4} Minel GÜL , ¹ Ahmet CAN , ² Harun GÜL 

¹ Uzman Kataforez Yüzey Kaplama Sanayi, Bursa, Türkiye.

² Sakarya University of Applied Science, Metallurgy and Material Engineering, Sakarya, Türkiye.

³ Bilecik Şeyh Edebali University, Chemical Engineering, Bilecik, Türkiye.

⁴ Bursa Technical University, Department of Chemistry, Bursa, Türkiye.

* Corresponding author, e-mail: y205012020@subu.edu.tr, <https://orcid.org/0000-0001-7557-9617>

Submission Date: 20.09.2023

Acceptation Date: 14.11.2023

Abstract

This study aims to improve the corrosion properties of (AISI 1040) materials used in the automotive industry. For this purpose, two different coating techniques were applied to the same surface. As part of the research, different passivation processes (transparent, blue, yellow, and black) were applied to alkaline Zn-Ni coatings. Geomet 321 and Geomet ML Black coatings were deposited on the passivation layer to form a double-layer coating. In order to investigate the adhesion and corrosion effects of these coatings, a dry adhesion test, a water test, a humidity test, and a salt spray test were carried out, and cross-cut adhesion tests were carried out after each corrosion test. After all these tests, rust formation was analysed by visual analysis, and atomic weight percentages and coating thicknesses were examined by X-ray. The transparent passivation after the Zn-Ni coating fully satisfied both adhesion and corrosion protection requirements for 321 and ML Black coatings. No red rust formation was observed on the coating samples after the test; only partial white rust formation was observed, and no peeling of the coating layer was detected in the adhesion tests. As a result, the optimum result of the passivation processes used for Geomet 321+ML Black coatings applied after the Zn-Ni + passivation process was obtained with transparent passivated Zn-Ni coatings. Even after 1200 hours, no red rust was observed in passivated Zn-Ni coating+ Geomet 321+ Geomet ML Black.

Keywords: Zinc-Nickel, Passivation, Geomet, Zink Flake, Corrosion

Farklı Pasivasyon İşlemlerinin Alkali Zn-Ni Kaplamalara Etkisi: Geomet 321 ve ML Black Kaplamaların Korozyon Direnci ve Yapışma Performansı

Özet

Bu çalışma, otomotiv endüstrisinde kullanılan malzemelerin (AISI 1040) korozyon özelliklerinin iyileştirilmesi amaçlanmıştır. Bu amaçla aynı yüzeye iki farklı kaplama tekniği uygulanmıştır. Araştırma kapsamında Alkali Zn-Ni kaplamalara farklı pasivasyon işlemleri (şeffaf, mavi, sarı ve siyah) uygulanmıştır. Pasivasyon tabakası üzerine Geomet 321 ve Geomet ML Black kaplamalar ile kaplanarak; çift katmanlı bir kaplama tabakası oluşturulmuştur. Bu kaplamaların yapışma ve korozyon etkilerini incelemek için kuru yapışma, su, nem ve tuz püskürtme testleri gerçekleştirilmiş ve her bir korozyon testinden sonra Cross Cut Çapraz kesme testleri yapılmıştır. Tüm bu testlerden sonra kırmızı ve beyaz pas oluşumu görsel analiz ile, atomik ağırlık yüzdeleri ve kaplama kalınlıkları ise X-ray ile incelenmiştir. Zn-Ni kaplamada uygulanan şeffaf pasivasyon, 321 ve ML Black sonraki uygulanan kaplamalar için hem yapışma hem de korozyon koruma gereksinimlerini tam olarak karşılamıştır. Testten sonra kaplama numunelerinde kırmızı pas oluşumu gözlenmedi; sadece kısmi beyaz pas oluşumu gözlemlendi ve yapışma testlerinde kaplama katmanında sıyırılma tespit edilmemiştir. Sonuç olarak, Zn-Ni + Pasivasyon işlemi sonrası uygulanan Geomet 321+ML Black kaplamaları için kullanılan pasivasyon

¹ Corresponding author: Tel: 0 534 316 86 80
E-mail: y205012020@subu.edu.tr

işlemlerinden optimum sonuç; şeffaf pasifleştirilmiş Zn-Ni kaplamalar ile elde edilmiştir. 1200 saat sonunda bile kırmızı pas gözlenmemiştir.

Anahtar kelimeler: Çinko-Nikel, Pasivasyon, Geomet, Çinko Flake, Korozyon,

1. Introduction

The most common metals used in the automobile industry include steel, iron, and aluminium. Each metal has unique properties that make it ideal for different automotive parts. Their low resistance to corrosive environments limits some of their uses. Corrosion that starts at a tiny point on the surface of the metal progresses to the inner parts of the metal over time, and rusting occurs. This reduces the service life of the metal. Corrosive wear resistance can be increased by coating the metal with different techniques (galvanizing [1], hot dip [2], electrodeposition [3], electroless [4]).

Zinc plating is widely used to protect materials used in structural and engineering applications. These coatings provide good corrosion resistance as well as good mechanical properties for the material. On the other hand, a high dissolution rate limits the applications of zinc coatings. The life of zinc coatings can be extended by phosphating and passivating with trivalent chromium (Cr^{+3}). The corrosion resistance of zinc can be significantly improved by alloying with transition metals such as Ni, Co, Sn and Cr [5].

Zinc is a silver-white metal that is soluble in acid and alkaline solutions and is brittle at room temperature. Zinc carbonate may form on the zinc surface with humid air and this slowing down corrosion [6], [7]. The standard electrode potential of zinc is -0.762 V , which is more negative than iron (-0.447 V) [6]. Therefore, zinc is used as anode dissolution to protect the steel substrate from corrosion [8] [9]. Zinc coating thicknesses of $6\text{-}12\ \mu\text{m}$ are sufficient in dry weather conditions, whereas zinc coating thicknesses of $15\text{-}20\ \mu\text{m}$ are required in humid conditions [10]. Zinc plating baths can be basically divided into two categories as cyanide and non-cyanide baths. Cyanide zinc solutions have a faster and better dispersion capacity on the surface. However, cyanide is toxic and dangerous for human health [11]. Therefore, cyanide-free baths are preferred for obtaining zinc thin films. Chloride zinc technology is a typical type of cyanide-free zinc coating with many advantages [12]. Some researchers have investigated using chloride zinc technology to make zinc thin films [13]. Weak acid electrolytes give deposits with the desired nickel content (about $12\text{-}17\%$ Ni) with high current efficiency, but the dispersion of the plated metal is poor. In contrast, alkaline processes are less efficient but give more uniform plating, and the baths are non-corrosive [14]. Essential alkali baths usually contain Zn and Ni ions, an alkali metal hydroxide, and a complexing agent for nickel. In addition, brighteners and carrier chemicals are also used.

Zinc coatings are subjected to passivation treatment after coating because of their poor corrosion resistance in aggressive environments such as acid and alkaline. The chromate passivation process is widely used to further improve the corrosion resistance of zinc coatings. After passivating, an intensive film can be formed on the surface of the zinc plating to improve its corrosion resistance. The zinc surface has been passivated to prevent fingerprints and to enhance the surface. McLaren et al. reported in detail the passivation technology of +6 valence chromium for zinc [15]. However, due to its toxicity, hexavalent chromium used in passivation is restricted in many industrial sectors. Trivalent chromium is like hexavalent chromium in many ways, but its toxicity is only 1% of that of hexavalent chromium [14]. During the passivation process, zinc begins to dissolve by anodic dissolution, and a reaction occurs between zinc and chromate ions. During the passivation process, zinc begins to dissolve by anodic dissolution and a reaction occurs between zinc and chromate ions. As a result of this reaction, zinc forms a barrier layer called zinc chromate, which is resistant to moisture and air [16]. Water is absorbed when the passivation layer is scratched or mechanically damaged, and the damaged area is repaired [17]. The zinc chromate layer prevents anionic oxidation of the substrate surface by preventing interaction with oxygen, thus supporting the durability and longevity of the zinc coating. Zn^{2+} and Cr^{3+} hydroxide precipitates can be obtained at higher interfacial pH, which directly contributes to forming the dense passivating layer. The trivalent chromium passivation of zinc can be broadly categorized into transparent, blue, yellow, black. The trivalent chromium passivation of zinc can be broadly categorized into transparent, blue, yellow, black. There is a great demand for the development of trivalent chromium passivation technology for zinc coating with the development of environmental protection. However, the component of trivalent chromium passivation solution is more complex and less stable compared to hexavalent chromium passivation solution [18]. Cr^{+3} passivation baths are organic (resin), or inorganic (silicate) based.

This study investigated trivalent chromium transparent, blue, yellow, and black passivation technology to improve the corrosion resistance of Zn-Ni coatings. In addition, non-passivated Zn-Ni coating samples were produced for comparison. Then, organic lamellar zinc coatings were made on passivated and non-passivated coatings. Alkaline zinc-nickel alloy coating, Geomet 321 and ML Black processes are applications to improve corrosion performance. This study will test Alkali Zn-Ni alloy coating + Geomet 321, and Alkali Zn-Ni alloy coating + ML Black, and their effects on corrosion resistance will be investigated. For this research, five different tests were carried out: Crosscut (dry adhesion), moisture resistance, water resistance and salt spray.

2. Materials and Methods

Zinc alloy coating produced were carried out to investigate the effect of different passivation applications on the corrosion resistance of zinc alloy coatings. Geomet 321 and Geomet ML Black coatings were produced after the passivation process was applied on the zinc coating surface, aiming to improve the tribological properties. This study used 10x15 cm sheet plates (AISI 1040) as coating substrate. Coating bath and parameters are presented in Table 1. After the coating baths were prepared, analyses were performed, and the coating procedure was started according to the positive analysis results. The analyses are presented in Table 3. A model of the coating layers is presented in Figure 1 and the process flow in Figure 2. Each of the coatings was carried out in 100 L baths.

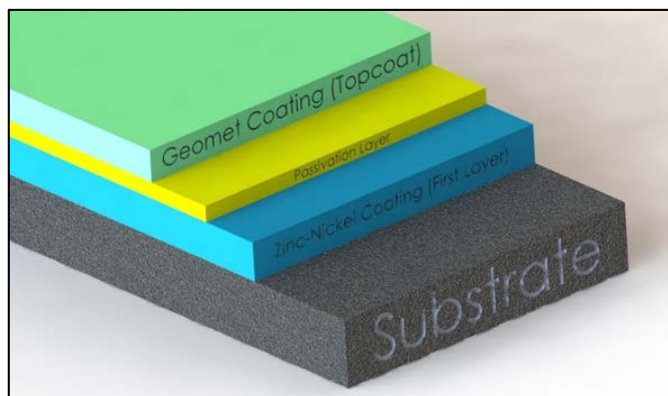


Figure 1. Coating layer model.

Firstly, metal materials were subjected to pre-treatment procedure and Zn-Ni alloy coatings were applied on them. Twenty-five pieces of Zn-Ni were coated with a 5-10 μm coating thickness. After coating, five pieces each of non-passivated, transparent, blue, yellow, and black passivated coatings were produced and the effects of passivation on the adhesion strength and corrosion properties of Geomet 321 and Geomet ML Black coatings were investigated in detail.

Table 1. Concentration of Zn-Ni coating bath.

BATH VOLUME	BATH CHEMICALS CONCENTRATION				
	Potassium Hydroxide (caustic)	ZnO (Zinc Oxide)	A Plus (Support)	B Plus (Nickel Feed)	C Plus (Polisher)
100 L	17 kg	1 kg	8 L	1,2 L	0,5 L
BATH PARAMETERS					
Temperature ($^{\circ}\text{C}$)			25-35 (Should not exceed 35 $^{\circ}\text{C}$)		
Time (min.)			20		
Current (A/dm^2)			6		

In general, zinc coatings produced in high temperature baths were operated at room temperature (maximum 35 $^{\circ}\text{C}$) since some problems such as surface roughness were encountered. The type of passivation processes applied after coating and the number of samples produced are presented in detail in Table 2. Geomet 321 and ML Black coatings were applied to the Zn-Ni coating surfaces after passivation process.

Table 2. Counts of passivation and samples performed after Zn-Ni coating.

PASSIVATION	SAMPLE QUANTITY (Zn-Ni)
Non-Passivation	5
Transparent Passivation	5
Blue Passivation	5
Yellow Passivation	5
Black Passivation	5
TOTAL	25

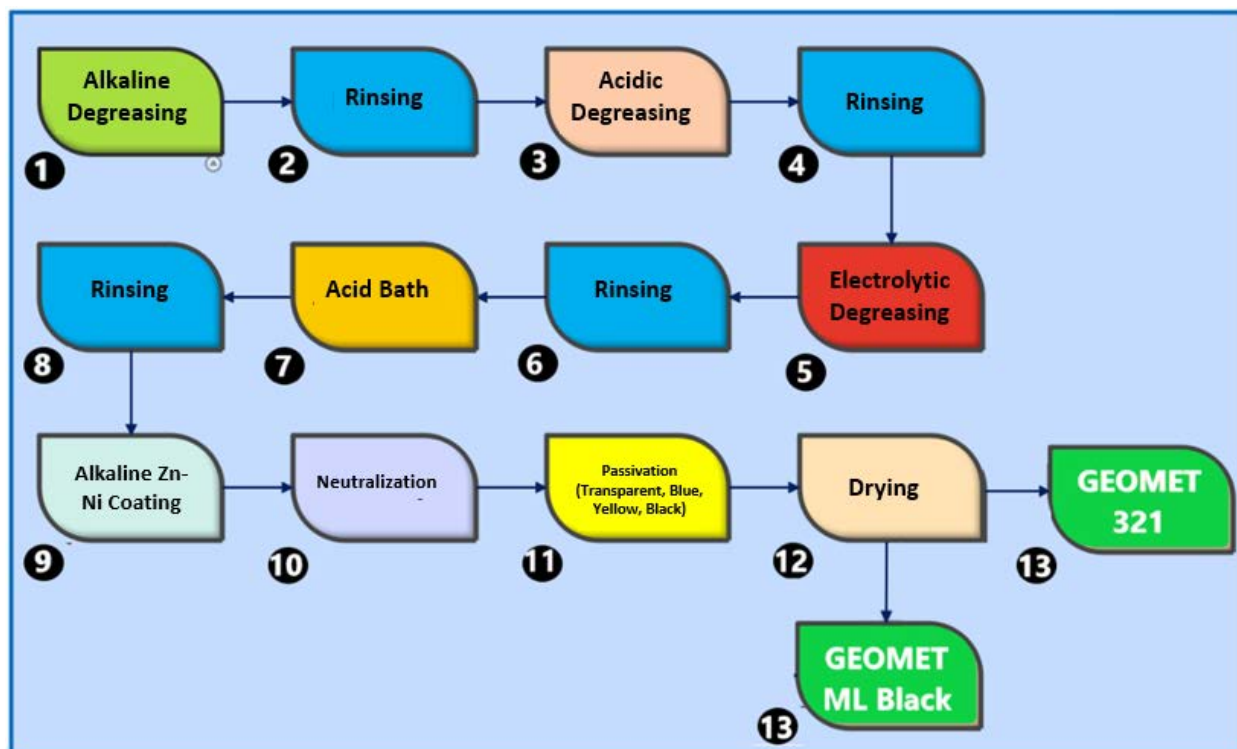


Figure 2. Production flow card.

Alkaline, acidic, and electrical degreasing processes were carried out to remove impurities on the sample surface before coating. The alkaline degreasing bath consisted of chemicals containing powder caustic and surfactant, and the procedure was carried out at 60 °C for 15 minutes. After rinsing, acidic degreasing was used to remove rust from the metal surface. The acidic degreasing bath consisted of sulphuric, hydrofluoric, and nitric acid. Acidic degreasing was carried out for 15 seconds at room temperature. The samples were rinsed again, and the electrical degreasing (alkaline) procedure with surfactant was started. In cathodic cleaning, the sample to be cleaned is connected as a cathode and current is passed in the electrolyte. The hydrogen gas generated by the current is scrubbed and stirred, and the sample surface is cleaned in detail. The samples were rinsed again and immersed in a hydrochloric solution at 31% concentration. At this point, dilute acid was used to neutralize the surface of the substrate. After final rinsing, alkaline Zn-Ni plating was started, which concentration and parameters are given in Table 1. After coating, the neutralization process was carried out. This process is applied to reduce the effect of chemicals remaining from the coating bath on the surface of the material, to clean the residues, to prevent oxidation and to maintain the pH balance on the surface. After rinsing, it was neutralized with a 5-6% weak acid to neutralize the alkalinity completely.

Once the concentration and convenience of the contents were achieved, the coating processes were carried out by pre-treating the sample in Figure 2. The baths prepared before coating were analysed using the methods given in Table 3. The amount of caustic must always be much higher than the amount of ZnO. Because this caustic content, which is more than the amount required to react with zinc oxide, prevents zinc oxide from precipitating. In the cyanide-free method, the reduction of Zn^{+2} ions occurs after this reaction chain. The amount of zinc and caustic is determined according to the bath volume. The amount of zinc oxide (ZnO) should be between 5 and 10 g/L, while the amount of sodium hydroxide (NaOH, caustic) should be between 120 and 140 g/L. The zinc oxide is dissolved by the heat given off by the caustic. This solution is added to the bath after cooling. Organic substances are added during the cooling phase and the bath volume is completed. At this stage the presence of free Zn^{+2} ions in the solution are important for the plating process. Especially in a cyanide-free process, the reduction of Zn^{+2} ions takes place in the last step of this reaction chain.

Table 3. Analyses performed in the baths prepared before coating.

ALKALINE Zn-Ni BATH ANALYSIS	<ol style="list-style-type: none"> 1.) Add 5 mL zinc bath solution to 100 mL distilled water. 2.) Add 35 mL of pH 4,2 buffer solution. 3.) Add 3-5 drops of Xylenol orange indicator. 4.) Titrated with 0,1 M EDTA until the color changed from red to yellow. 5.) The consumption is obtained by multiplying by 1,31.
ALKALINE Zn-Ni CAUSTIC ANALYSIS	<ol style="list-style-type: none"> 1.) Add 5 mL zinc bath solution to 100 mL distilled water. 2.) 20 mL BaCl₂ solution is added in solution. 3.) 3-5 drops of phenolphthalein indicator are added. 4.) Titrate with 1 N HCl until the pink colour disappears. 5.) The consumption is obtained by multiplying by 8.
ZINC ALKALINE DEGREASING BATH ANALYSIS	<ol style="list-style-type: none"> 1.) Add 2 mL of electrolyte from zinc bath to 50 mL of distilled water. 2.) Add 2-3 drops of methyl rhodamine indicator. 3.) Titrate with 0,1 N HCl. The colour changes from orange to red. 4.) The consumption is obtained by multiplying by 0,27.

Passivation has been applied to prevent fingerprints and improve properties on zinc coated surfaces, to give the surfaces a decorative appearance and to increase the corrosion resistance of the coating. Passivation is the process of depositing a protective chromate layer on metal. Zinc chromate layer is formed by anodic dissolution of zinc and reaction of zinc and chromate ions. The conversion of oxygen to anion oxide inhibits electrochemical phenomena and increases corrosion protection [19]. Passivation baths are chromium based and Cr⁺³ ions are used in the baths. The use of Cr⁺⁶ ions is banned in many industries due to their toxicity to nature. [20]. The passivation layer has decorative colours according to the applied formulation. In addition, transparent, blue, yellow, and black colored protection layer can be applied to this layer to increase corrosion resistance. These protection baths are organic (resin) or inorganic (silicate) based. During this process, the metal surface is made in an acidic or basic solution. This solution dissolves the oxide layer on the surface and forms a more durable passivation layer. The bath parameters of all passivation processes are presented in Table 4. As a final process after passivation, drying was carried out for 10 minutes at 80 °C.

Table 4. Passivation types and applied parameters.

PASSIVATION TYPE	TEMPERATURE (°C)	TIME (Sec.)	PH	Cr CONCENTRATION (g/L)
Transparent	28	30	1,5-2	0,80 - 1,01
Blue	28	60	1,5-2	1,1-3
Yellow	Room Temperature	60	1,8-2	9-11
Black	28	40	1,8-2	1,2-1,4

Carbonates, which cause a decrease in the conductivity of the solution, increase in the solution with the temperature of the solution and the stirring of the solution, which causes an inhibition of the electroplating process. The acceptable amount of carbonates in the solution varies between 50 and 100 g/L, which is the usual range of the amount of CO₂ absorbed from the air. There are many methods of precipitating and removing carbonates from the solution. The first technique is to cool the solution down to 5 - 10 °C until the carbonates freeze and then to filter the carbonates out of the solution. A less commonly used method is to precipitate the carbonates with calcium hydroxide [19]. The effect on the corrosion resistance of Geomet 321 and ML Black coatings produced after different passivation treatments for Zn-Ni coatings was investigated.

3. Results and Discussions

All the passivation types described were applied after Zn-Ni plating and the surface images are shown in Figure 3. When the surface images are examined, the presence of passivation formed after Zn-Ni coating can be clearly observed on the surface. The layer thicknesses and atomic distributions (%) obtained by X-ray after passivation are given in Table 5. Considering the atomic weights and layer thicknesses, the %Ni ratio of the non-passivated layers is lower compared to the passivated layers. It can be said that the %Ni ratio is maintained after passivation. While the thickness of the non-passivated layer was 6.7 µm, the thickness of the transparent, the blue and the yellow passivated layers increased, respectively. For the black passivation, the film thicknesses decreased again. When Table 4 is analysed can be said that the amount of Cr in the bath and the passivation times are effective.

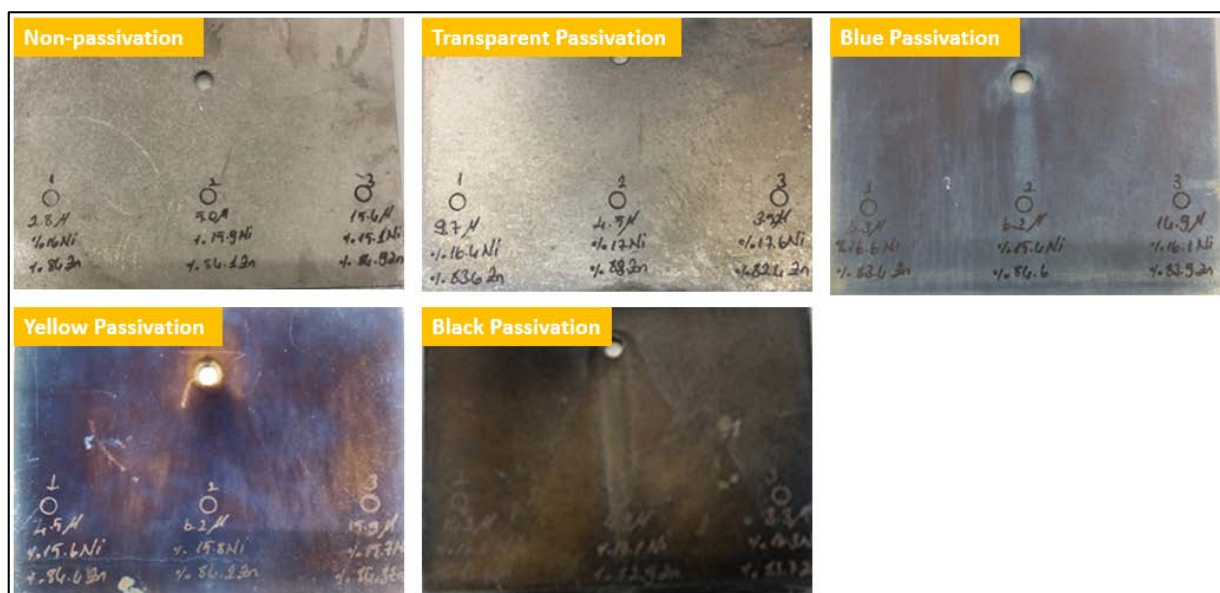


Figure 3. Surface images of different passivation layers applied after coating.

Table 5. Coating thickness and (%) atomic weight obtained after passivation with X Ray device.

PASSIVATION TYPE	% Ni	% Zn	COATING THICKNESS (μm)
Non-passivation	15,7	84,3	6,7
Transparent	15,8	84,2	7,8
Blue	16	84	8,5
Yellow	17,1	82,9	8,9
Black	16,6	83,4	7,6

For zinc-nickel alloy coatings, the nickel ratio in the alloy should be between 15-16%, above 16% the cathodic protection effect is reversed, and an anodic corrosion effect is caused. In other words, an alloy ratio greater than 16% will cause the coated part to show red rust in a much shorter time than expected [21]. The following coding system has been used to facilitate understanding of the coatings in the text and images.

Table 6. Coding system of produced coatings.

CODE		CODE	
Zn-Ni-321	Zinc Nickel + Geomet 321 (non-passivation)	Zn-Ni-ML	Zinc Nickel + ML Black (non-passivation)
Zn-Ni-Transparent-321	Zinc Nickel + Transparent Passivation + Geomet 321	Zn-Ni-Transparent-ML	Zinc Nickel + Transparent Passivation + ML Black
Zn-Ni-Blue-321	Zinc Nickel + Blue Passivation + Geomet 321	Zn-Ni-Blue-ML	Zinc Nickel + Blue Passivation + ML Black
Zn-Ni-Yellow-321	Zinc Nickel + Yellow Passivation + Geomet 321	Zn-Ni-Yellow-ML	Zinc Nickel + Yellow Passivation + ML Black
Zn-Ni-Black-321	Zinc Nickel + Black Passivation + Geomet 321	Zn-Ni-Black-ML	Zinc Nickel + Black Passivation + ML Black



When a zinc-coated part starts to oxidize, it is first covered with a white layer for when consist of white zinc oxide (ZnO) [22]. After all the zinc has been oxidized, the iron begins to oxidize, and its color becomes red [23]. Therefore, the white rust resistance defines the performance of the passivation layer, and the red rust value defines the performance of the zinc layer. Most red rust metals (Fe_2O_3) occur as compounds in nature. Metals or alloys are formed by adding materials to these compounds. These formed metals or alloys tend to return to their stable state, the compound state.

After the preparation of the organic zinc lamellar coatings, the weights of the coatings were measured with an X-ray and the results of the weights of the coatings with different passivation processes are given in Table 6. Since the lamellar coating is not a homogeneous coating, a wide shear gap is observed. It was observed that the parts which were expected 24 g/m^2 in a 2-layer zinc flake coating had very high coating weights. The measurements were evaluated as Zn-Ni + Geomet coating weight, as both types of coating used to coat the substrates are zinc containing. Table 7 shows the weights of the coatings in g/m^2 according to the passivation type.

Geomet 321; The lowest weight of 59.2 g/m² was obtained with Zn-Ni+ Geomet 321 coating non-passivation. This value increased to 76.3 g/m² with transparent passivation. The highest film thickness was obtained in the transparent passivation layer. Coating weights of 65.5, 69.3 and 60.8 g/m² were obtained with blue, yellow, and black passivation respectively.

Geomet ML Black; While 35.1 g/m² was observed for the non-passivated Zn-Ni+ Geomet ML Black coating, this value increased to 48.7 g/m² for the transparent passivation, the highest observed. For the other types of passivation, coating weights of 44.4, 47.8 and 36.2 g/m² were observed for blue, yellow, and black respectively. The highest value was again observed for the transparent passivation when comparing the thickness of Geomet 321 and ML Black.

Table 7. [Zn-Ni Coating+ Geomet Coating] weight obtain by X Ray.

PASSIVATION TYPE		
	ALKALINE Zn-Ni + GEOMET 321	ALKALINE Zn-Ni + GEOMET ML BLACK
Non-passivation	59,20 g/m ²	35,10 g/m ²
Transparent	76,30 g/m ²	48,70 g/m ²
Blue	65,50 g/m ²	44,40 g/m ²
Yellow	69,30 g/m ²	47,80 g/m ²
Black	60,80 g/m ²	36,20 g/m ²

3.1 Cross-Cut/ Dry Adhesion Test

Before and after corrosion, good adhesion of coatings with different passivation processes to the substrate surface is essential. The reason for this is that the mechanical and tribological properties of the material can be adversely affected if a coating is easily detached from the surface of the substrate. Cross-cut (dry adhesion) tests were performed on coatings with different passivation processes to assess this adhesion resistance. Figure 4 compares the surface images of the coatings with different passivation processes after the cross-cut test. Table 8 also shows the test results of Zn-Ni+ Geomet coatings with different passivation treatments after dry bonding. Analysis of the images shows that the Zn-Ni coating successfully passed the dry adhesion test of all Geomet 321 and Geomet ML Black coatings with no passivation, transparent, blue, and yellow passivation processes. However, the Geomet 321 coating with black passivation passed the dry adhesion test, while the Geomet ML Black coating failed due to high peeling after the test.

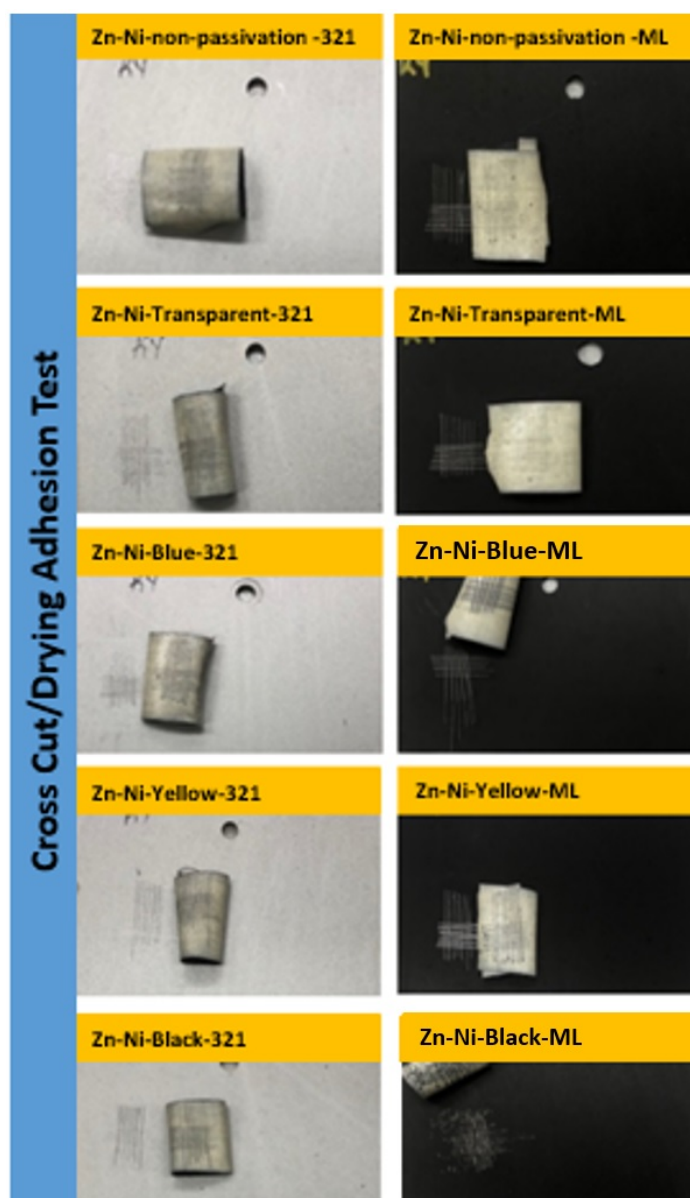


Figure 4. Dry adhesion tests of coatings produced in different passivation processes.

Water resistance, moisture resistance and salt spray resistance tests were not performed as the samples with ML Black Geomet applied over alkaline Zn-Ni + Black passivation failed the dry adhesion test.

Table 8. Dry post-adhesion test results for ML Black and 321 coatings for passivation applied to Zn-Ni coatings.

Zn-Ni (DRY ADHESION)	GEOMET 321	GEOMET ML Black
Non-passivation	✓	✓
Transparent Passivation	✓	✓
Blue Passivation	✓	✓
Yellow Passivation	✓	✓
Black Passivation	✓	X

3.2 Water Resistance Test

The water resistance test was performed according to ASTM D 870-02. All coating samples were soaked in deionised water at a constant temperature of 40°C for 48 hours. At the end of this time, the part was removed from the water, dried with blotting paper, and kept in ambient conditions for two hours. After this time, it was subjected to an adhesion resistance test. After the peel test, no change in the colour of the coating is expected. Figure 5 shows the surface image of the adhesion test results after the water resistance test. Table 9 also shows the results of the adhesion test of the coatings

with different passivation treatments after the water resistance test. According to the adhesion test results, the blue passivated Geomet 321 and yellow passivated Geomet ML Black coatings failed the test.

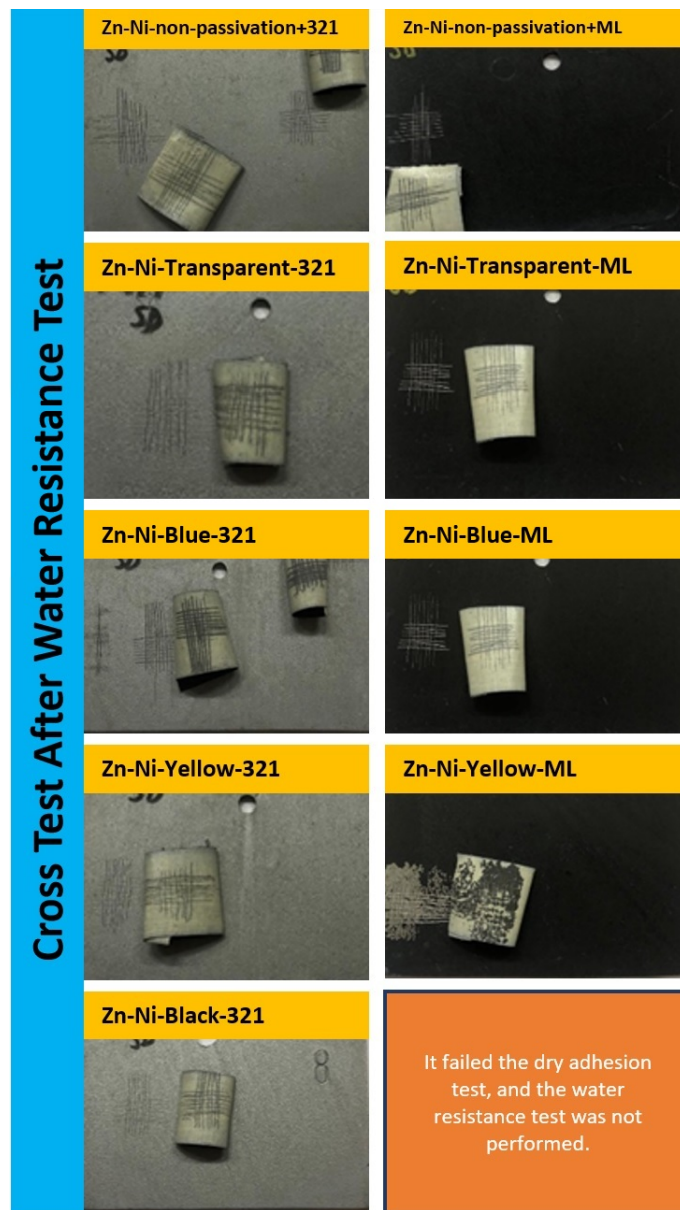


Figure 5. Surface images of adhesion test conducted after water resistance test.

The adhesion test was carried out after the water resistance test. Moisture and salt spray tests were not performed on Geomet ML Black applied over alkaline Zn-Ni + Yellow Passivation because these coatings failed the dry adhesion test.

Table 9. The results according to the adhesion test performed after the water resistance test.

Zn-Ni (WATER TEST)	GEOMET 321	GEOMET ML Black
Non-passivation	✓	✓
Transparent Passivation	✓	✓
Blue Passivation	X	✓
Yellow Passivation	✓	X
Black Passivation	✓	It failed the dry adhesion test, and the water resistance test was not performed.

3.3 Moisture Resistance Test

High humidity results in oxidation of metals, enhanced chemical reactions and chemical or electrochemical breakdown of organic and inorganic surface coatings. Humidity influences the surface properties of the material. Effects include swelling of the material due to moisture absorption, loss of physical strength of the material, loss of electrical and thermal insulation properties, change in flexibility or plasticity. MIL-STD-810G Method 507.5 described a test method for determining the resistance of a material to the effects of a hot and humid atmosphere. Hot and humid conditions are generally found year-round in tropical regions and seasonally in mid-latitude areas. In these regions, moisture damage occurs primarily in materials exposed to changes in pressure, temperature, and relative humidity [24]. Figure 6 shows the surface images of Geomet 321, and ML Black coatings applied after the different passivation processes following the moisture resistance test. Table 10 shows the test results of coatings with different passivation processes after the moisture resistance test. The coatings that were not passivated for Geomet 321 and blue passivated for ML Black failed the adhesion test after moisture resistance. They were not included in the salt spray test.

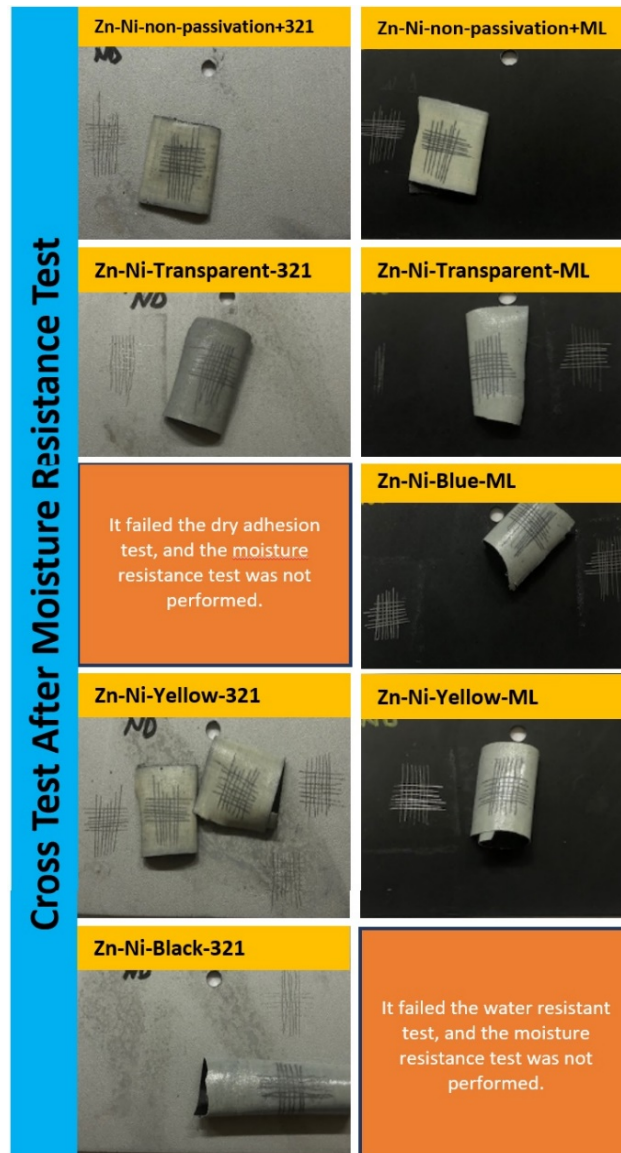


Figure 6. Surface images after coating adhesion test of different passivation treatments applied after moisture resistance test.

Moisture resistance was followed by the adhesion test. The parts with the Geomet ML Black Geomet applied over the alkaline Zn-Ni + Black passivation unsuccessful the dry adhesion test. Therefore, the salt spray was not carried out to this samples.

Table 10. Test results of coatings with different passivation treatments after moisture resistance test.

Zn-Ni (MOISTURE TEST)	GEOMET 321	GEOMET ML Black
Non-passivation	X	✓
Transparent Passivation	✓	✓
Blue Passivation	Because it failed the water resistance test, it was not subjected to the moisture resistance test.	X
Yellow Passivation	✓	Because it failed the water resistance test, it was not subjected to the moisture resistance test.
Black Passivation	✓	It failed the dry adhesion test, and the water resistance test was not performed.

3.4 Salt Spray Test

This test is used to determine the resistance of the protective coatings and surfaces of the sample to the effects of salt. The samples are placed in the test chamber and exposed to the salt spray. When the test is completed, the specimen is subjected to physical, electrical, and corrosive tests and any defects recorded [25].

Due to high white rust formation, Zn-Ni+ ML Black and Zn-Ni+ Geomet 321 coatings without passivation treatment failed the salt spray test. The other samples passed the test. Figure 7 shows the surface images of the coatings with different passivation processes after the salt spray test. The results of the salt spray test are shown in Table 11. The surface images 321 and Black coatings without passivation showed a high rate of white rust after the test and therefore failed. The transparent passivated 321 and Black coatings showed no red rust and a very low level of white rust and passed the test. The samples were not included in the salt spray test for blue passivation as they had failed in the previous tests. In the yellow passivation application, 321 coating passed the salt spray test, while ML Black coating was not included in the salt spray test because it failed the water test. 321 coating passed the salt spray test, but ML Black coating failed the salt spray test.

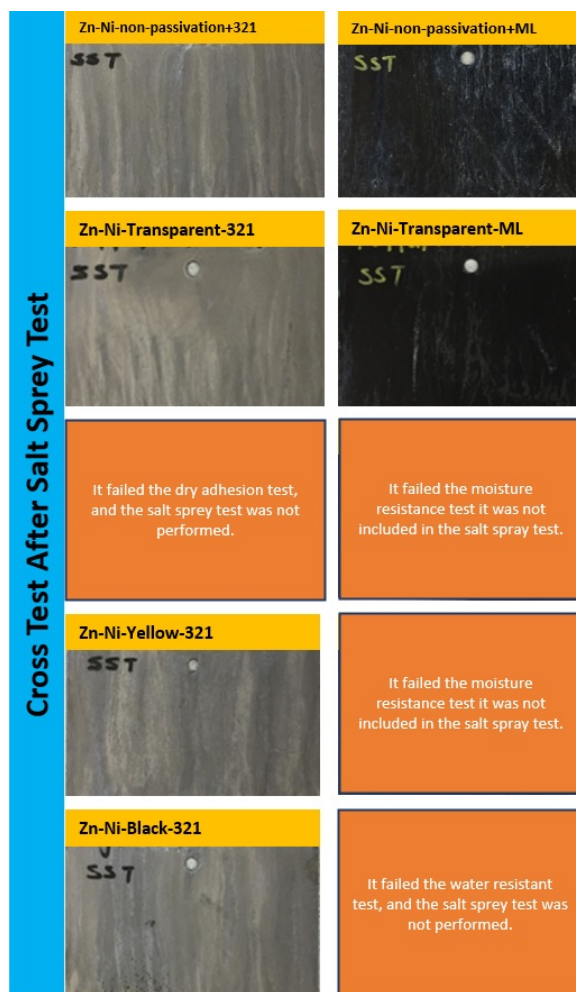


Figure 7. Surface images after salt spray test of coatings with different passivation.

Table 11. Geomet 321 and ML Black coatings salt spray test results after different passivation process.

Zn-Ni (SALT SPRAY TEST)	Geomet 321	Geomet ML Black
Non-passivation	X	X
Transparent Passivation	✓	✓
Blue Passivation	Because it failed the water resistance test, it was not subjected to the salt spray test.	Because it failed the moisture resistance test, it was not included in the salt test.
Yellow Passivation	✓	Because it failed the water resistance test, it was not subjected to the salt spray test.
Black Passivation	✓	It failed the water resistance test, and the salt spray test was performed.

Table 12 shows the corrosion resistance times after the salt spray test without red rust formation. According to these test results, Geomet 321 coatings showed corrosion resistance for 720 hours. In the same test, Zn-Ni coatings showed corrosion resistance for 1000 hours. Using these two coatings together, the combination of Zn-Ni + Geomet 321 provided 1200 hours of salt spray resistance. In addition, the combination of Zn-Ni + ML Black showed a slightly higher corrosion resistance with a salt spray resistance of 1500 hours. These results showed that the combination of the two coatings provided a higher corrosion resistance in the salt spray test.

Table 12. Durability times of different coatings after the salt spray test.

SALT SPRAY TEST (ISO 9227)	TIME (WITHOUT RED RUST)
Organic Zinc Lamellar Coating (Geomet-321) Corrosion Performance [25]	720 hours
Alkaline Zinc Nickel Coating (Zn-Ni) Corrosion Performance [26]	1000 hours
Organic Zinc Lamellar (Geomet 321) + ML Black Corrosion Performance [25]	1008 hours
Zn-Ni Coating +Geomet-321 Corrosion Performance [26]	1200 hours
Zn-Ni Coating+ ML Black Corrosion Performance [26]	1500 hours

4. Conclusions

Corrosion performance has been improved by combining organic zinc lamella plating with alkaline Zn-Ni coating. As a result, a new process with high corrosion resistance was obtained by using two different processes in a single process. Given that the corrosion resistance of the lamellar coating is high, a new process has been developed that can exceed this level. All different passivation samples passed the dry adhesion test except for ML Black coating over alkaline Zn-Ni+ black passivation.

The alkaline Zn-Ni + blue passivation + Geomet 321 and ML Black Geomet over alkaline Zn-Ni + yellow passivation sample failed the water resistance test. Except for this sample, the coated parts successfully passed the water resistance test. The samples passed the water resistance test with an alkaline Zn-Ni coating + passivation over Geomet 321 coating. The moisture resistance test was failed by the non-passivated alkaline Zn-Ni+321 coating sample and the blue passivated Zn-Ni+ ML Black coatings.

In the salt spray test, the samples that passed the test passed the test for Geomet 321 for the transparent, yellow and black passivation, while the samples with the other passivation failed the test. For ML Black only the transparent passivation passed the test. In the salt spray tests, no red rust was observed on any of the samples, only white rust caused by zinc. Therefore, white rust rates were considered for comparison. It can be said that all samples passed the test if red rust is considered. Red rust was not observed in any of the samples.

Substrates coated with 321 Geomet over alkaline zinc nickel + passivation showed no red rust even after 1200 hours. Besides, no red rust formation was observed on the parts coated with ML Black at the end of 1500 hours.

When the Zn-Ni alloy coatings with ML Black were analysed, it was found that the coatings with non-passivation, with blue passivation, with yellow passivation and with black passivation failed pass the tests. Coatings without passivation and blue passivation failed the test with 321 Geomet. The main reason for the poor adhesion of ML Black coating to the surface after Zn+ Ni passivation and the high failure rate in the corrosion tests is that ML Black coating has a lower deposition rate than Geomet 321.

Based on the tests carried out on the Geomet coating process to be carried out on Zn-Ni+ passivation, the process that should be preferred is to produce Geomet 321 coatings on Zn-Ni alloyed coating. Transparent passivation + Geomet 321 and Geomet ML Black coatings applied after Zn-Ni coating with different passivation processes passed all tests.

Peer-review: Externally peer - reviewed.

Author contributions: İbrahim USTA-Literature Search and Writing, Oğuz YILMAZ and Minel GÜL- Experimental Procedure and Tests.

Conflict of Interest: No conflict of interest was declared by the authors.

Appreciation: We would like to thank Uzman Kataforez for providing us with experimental application and testing opportunities.

Financial Disclosure: The authors declared that this study has received no financial support.

References

- [1] S. M. A. Shibli, B. N. Meena, and R. Remya, "A review on recent approaches in the field of hot dip zinc galvanizing process," *Surf Coat Technol*, vol. 262, pp. 210–215, Jan. 2015, doi: 10.1016/J.SURFCOAT.2014.12.054.
- [2] V. Jagannathan, "Emerging technologies in the hot-dip coating of automotive sheet steel," *JOM*, vol. 45, no. 8, pp. 48–51, Aug. 1993, doi: 10.1007/BF03222406/METRICS.
- [3] S. Tan, H. Algül, E. Kiliçaslan, A. Alp, H. Akbulut, and M. Uysal, "The effect of ultrasonic power on high temperature wear and corrosion resistance for Ni based alloy composite coatings," *Colloids Surf A Physicochem Eng Asp*, vol. 656, p. 130345, Jan. 2023, doi: 10.1016/J.COLSURFA.2022.130345.
- [4] H. Gul and İ. Usta, "Effect of Alumina Concentration on Morphology, Wear, and Corrosion: Electroless Ni-W-P/Al₂O₃ Composite Coatings on Aluminum Surfaces," *J Mater Eng Perform*, vol. 32, no. 13, pp. 6107–6122, Jul. 2023, doi: 10.1007/S11665-023-08184-X/TABLES/2.
- [5] S. Rajendran, S. Bharathi, and T. Vasudevan, "The Electrodeposition of Zinc-Nickel Alloy from a Cyanide-free Alkaline Plating Bath," <http://dx.doi.org/10.1080/00202967.2000.11871324>, vol. 78, no. 3, pp. 129–133, 2017, doi: 10.1080/00202967.2000.11871324.

- [6] X. L. Shang, B. Zhang, E. H. Han, and W. Ke, "Effect of small addition of Mn on the passivation of Zn in 0.1 M NaOH solution," *Electrochim Acta*, vol. 56, no. 3, pp. 1417–1425, Jan. 2011, doi: 10.1016/J.ELECTACTA.2010.10.067.
- [7] B. Sundaresan, A. Vasumathi, K. Ravichandran, P. Ravikumar, and B. Sakthivel, "Annealing effect on physical properties of spin coated ZnO films," <http://dx.doi.org/10.1179/1743294412Y.0000000016>, vol. 28, no. 5, pp. 323–328, Jun. 2013, doi: 10.1179/1743294412Y.0000000016.
- [8] P. Vany, "Standard Potentials in Aqueous Solutions," *J. Phys. Chem. Ref. Data*, vol. 18, pp. 1–21, 1978.
- [9] M. Mokaddem, P. Volovitch, and K. Ogle, "The anodic dissolution of zinc and zinc alloys in alkaline solution. I. Oxide formation on electrogalvanized steel," *Electrochim Acta*, vol. 55, no. 27, pp. 7867–7875, Nov. 2010, doi: 10.1016/J.ELECTACTA.2010.02.020.
- [10] T. V. Byk, T. V. Gaevskaia, and L. S. Tsybul'skaya, "Effect of electrodeposition conditions on the composition, microstructure, and corrosion resistance of Zn–Ni alloy coatings," *Surf Coat Technol*, vol. 202, no. 24, pp. 5817–5823, Aug. 2008, doi: 10.1016/J.SURFCOAT.2008.05.058.
- [11] N. S. Shifrin, B. D. Beck, T. D. Gauthier, S. D. Chapnick, and G. Goodman, "Chemistry, Toxicology, and Human Health Risk of Cyanide Compounds in Soils at Former Manufactured Gas Plant Sites," *Regulatory Toxicology and Pharmacology*, vol. 23, no. 2, pp. 106–116, Apr. 1996, doi: 10.1006/RTPH.1996.0032.
- [12] P. K. Leung, C. Ponce-De-León, C. T. J. Low, and F. C. Walsh, "Zinc deposition and dissolution in methanesulfonic acid onto a carbon composite electrode as the negative electrode reactions in a hybrid redox flow battery," *Electrochim Acta*, vol. 56, no. 18, pp. 6536–6546, Jul. 2011, doi: 10.1016/J.ELECTACTA.2011.04.111.
- [13] O. Kozaderov, J. Światowska, D. Dragoe, D. Burliaev, and P. Volovitch, "Effect of Cr(III) passivation layer on surface modifications of zinc-nickel coatings in chloride solutions," *Journal of Solid State Electrochemistry*, vol. 25, no. 4, pp. 1161–1173, Apr. 2021, doi: 10.1007/S10008-021-04898-X/FIGURES/9.
- [14] A. Urtiaga, E. Bringas, R. Mediavilla, and I. Ortiz, "The role of liquid membranes in the selective separation and recovery of zinc for the regeneration of Cr(III) passivation baths," *J Memb Sci*, vol. 356, no. 1–2, pp. 88–95, Jul. 2010, doi: 10.1016/J.MEMSCI.2010.03.034.
- [15] K. G. McLaren, J. H. Green, and A. H. Kingsbury, "A radiotracer study of the passivation of zinc in chromate solution—I," *Corros Sci*, vol. 1, no. 1–2, pp. 161–IN13, Jan. 1961, doi: 10.1016/0010-938X(61)90022-1.
- [16] T. Bellezze, G. Roventi, and R. Fratesi, "Electrochemical study on the corrosion resistance of Cr III-based conversion layers on zinc coatings," *Surf Coat Technol*, vol. 155, no. 2–3, pp. 221–230, Jun. 2002, doi: 10.1016/S0257-8972(02)00047-6.
- [17] P. L. Hagans and C. M. Haas, "Chromate Conversion Coatings," *Surface Engineering*, pp. 405–411, 1994, doi: 10.31399/ASM.HB.V05.A0001275.
- [18] Y. D. Yu, G. Y. Wei, J. W. Lou, H. L. Ge, L. X. Sun, and L. Z. Zhu, "Influence of bath temperature on zinc plating and passivation process," <http://dx.doi.org/10.1179/1743294412Y.0000000102>, vol. 29, no. 3, pp. 234–239, Apr. 2013, doi: 10.1179/1743294412Y.0000000102.
- [19] R. Berger, U. Bexell, T. Mikael Grehk, and S. E. Hörnström, "A comparative study of the corrosion protective properties of chromium and chromium free passivation methods," *Surf Coat Technol*, vol. 202, no. 2, pp. 391–397, Nov. 2007, doi: 10.1016/J.SURFCOAT.2007.06.001.
- [20] P. Sharma, S. P. Singh, S. K. Parakh, and Y. W. Tong, "Health hazards of hexavalent chromium (Cr (VI)) and its microbial reduction," <https://doi.org/10.1080/21655979.2022.2037273>, vol. 13, no. 3, pp. 4923–4938, 2022, doi: 10.1080/21655979.2022.2037273.
- [21] A. Can and L. Akyalçın, "Alkali Çinko Ve Alaşımli Çinko Kaplama Üzerine Çözücü Bazlı Çinko Lamelli Kaplama Uygulaması İle Oluşturulan Çok Katmanlı Kaplamanın Korozyon Önleme Performansı Üzerine Etkisinin İncelenmesi," *Eskişehir Osmangazi Üniversitesi Mühendislik ve Mimarlık Fakültesi Dergisi*, vol. 30, no. 2, pp. 300–308, Aug. 2022, doi: 10.31796/OGUMMF.1074520.
- [22] N. R. Short, A. Abibsi, and J. K. Dennis, "Corrosion resistance of electroplated zinc alloy coatings," <http://dx.doi.org/10.1080/00202967.1989.11870845>, vol. 67 pt 3, pp. 73–77, 2017, doi: 10.1080/00202967.1989.11870845.
- [23] I. Suzuki, Y. Hisamatsu, and N. Masuko, "Nature of Atmospheric Rust on Iron," *J Electrochem Soc*, vol. 127, no. 10, pp. 2210–2215, Oct. 1980, doi: 10.1149/1.2129376/XML.

- [24] “Nem Testi (MIL-STD-810G Metod 507.5).” Accessed: Sep. 15, 2023. [Online]. Available: [https://www.laboratuvar.org/endustriyel/mil-std-810g-testleri/nem-testi-\(mil-std-810g-metod-5075\)/](https://www.laboratuvar.org/endustriyel/mil-std-810g-testleri/nem-testi-(mil-std-810g-metod-5075)/)
- [25] “GEOMET® Protection Principals”, Accessed: Sep. 15, 2023. [Online]. Available: www.nofmetalcoatings.com
- [26] “Zinc-Nickel Electroplating Services | Plating Services | SPC.” Accessed: Sep. 15, 2023. [Online]. Available: <https://www.sharrettsplating.com/coatings/zinc-nickel>

Effects of Al-5Ti-0,2B and Al-5Ti-1B Grain Refiners on the Mechanical Properties of AA 1050 Aluminum Alloy

*^{1,2} Tuğçe Yunak , ¹ Erhan Duru , ² Samet Sevinç , ¹ Serdar Aslan 

¹ Sakarya University, Metallurgical and Materials Engineering, Sakarya, Turkey.

² ASAŞ Alüminyum San. A.Ş., Sakarya, Turkey.

* Corresponding author, e-mail: tugce.yunak1@org.sakarya.edu.tr, <https://orcid.org/0000-0002-4576-3779>

Submission Date: 24.11.2023

Acceptation Date: 05.12.2023

Abstract - This study investigates the effect of grain refiners on aluminum alloys and reveals important results for various industrial applications. In this work, twin roll casting method was used to produce aluminum sheets. The research then goes into the microstructure and mechanical investigation of 1050 aluminum alloy with two different grain refiners, Al-5Ti-0.2B and Al-5Ti-1B. Optical microscopy, SEM, tensile tests and hardness measurements were carried out in order to compare microstructural and mechanical properties of the alloys. As a result, obvious effects of the higher amount of boron in the Al-5Ti-1B alloy observed. According to the SEM analysis, it was clearly seen that homogeneous intermetallic phase distribution observed in the case of usage Al-5Ti-1B grain refiner. In addition to this reduction in grain sizes determined via optical microscope. This reduction in grain size result in increase in mechanical properties namely yield strength increased from 75MPa to 84 MPa, tensile Strength increased from 97 MPa to 102 MPa, hardness in brinell increased from 27 HB to 30 HB and brinell in Vickers increased from 32,9 HV to 38,2 HV. The observed improvements in mechanical properties and microstructure reveal the applicability of anodizing process to the materials that are produced by TRC casting.

Keywords: Al-5Ti-1B, Twin-Roll Casting, Grain Thinners, Boron

Al-5Ti-0,2B ve Al-5Ti-1B Tane İncelticilerin AA 1050 Alüminyum Alaşımının Mekanik Özellikleri Üzerine Etkileri

Öz – Bu kapsamlı çalışma, tane incelticilerin alüminyum alaşımlarının üzerindeki etkisini araştırmakta ve çeşitli endüstriyel uygulamalar için önemli çıkarımlar ortaya koymaktadır. Araştırmada, alüminyum levhalar üretimde hassasiyeti ve verimliliği ile tanınan ikiz merdaneli döküm metodundan yararlanılmıştır. Araştırma daha sonra Al-5Ti-0,2B ve Al-5Ti-1B olan iki farklı tane incelticili 1050 alüminyum alaşımının mikroyapı ve mekanik incelemesine girmektedir. Alaşımların mikroyapısal ve mekanik özelliklerini karşılaştırmak amacıyla optik mikroskop, SEM, çekme testleri ve sertlik ölçümleri yapılmıştır. Sonuçlar, Al-5Ti-1B alaşımında daha fazla bulunan borun belirgin etkisini ortaya çıkarmıştır. Bu alaşımı SEM analizinde incelediğimizde intermetalik yapıların azaldığını ve daha homojen bir yapının ortaya çıktığı net bir şekilde görülmüştür. Bunun ile birlikte optik mikroskop görüntülerinde tane boyutlarının küçüldüğü ve daha tanecikli bir yapı oluşmasına sebebiyet vermesinin yanında akma, çekme ve makro-mikro sertlik değerleri sırasıyla ortalama 75MPa, 97MPa, 27HB ve 32,9 HV ‘den 84MPa, 102MPa, 30HB ve 38,2HV ‘ye yükselmesi Al-5Ti-1B alaşımının mikroyapı ve mekanik özelliklerindeki iyileşmelerin net bir göstergesi haline gelmiştir. Mikroyapıda elde edilen bu gelişmeler ile özellikle ikiz merdane döküm tekniği ile üretilen malzemelerde eloksallama yüzey işleminin uygulanabilirliğini ortaya koymuştur.

Anahtar kelimeler: Al-5Ti-1B, İkiz Merdaneli Döküm, Tane İncelticiler, Bor

¹ Corresponding author: Tel: 0 530 664 33 47
e-mail: tugce.yunak1@org.sakarya.edu.tr

1. Giriş

Alüminyum, özellikle hafiflik işlenebilirlik, ısı-elektrik iletkenliği ve korozyona karşı üstün özellikleri nedeniyle otomotiv, havacılık, inşaat ve gıda gibi birçok sektörün vazgeçilmez haline gelmiştir [1].

Literatürdeki birçok çalışma, alüminyum bazlı alaşımların dökümünde daha üstün mekanik özellikler elde etmek için tane incelticiler kullanmıştır. Tane incelticiler, özellikle alüminyum alaşımlarında tane yapılarını inceleyebilmek için kullanılan katkı maddeleridir. Katılaşma işlemi sırasında kullanılan tane incelticiler ince ve eş eksenli tanelerin oluşumunu sağlayarak, mekanik özelliklerin iyileşmesinde yardımcı olurlar. Ayrıca tane inceltici kullanılmış alüminyum malzemelerde beslenme kabiliyetlerinin yüksek olması ile porozitesiz ve homojen bir yapının oluşması alüminyum malzemeler için avantaj sağlamaktadır [2], [3].

Alüminyum sektöründe Al-Ti, Al-B ve Al-Ti-B tane incelticileri yaygın olarak kullanılmaktadır. Titanyum partikülleri yeni çekirdeklenme bölgeleri sağlarken, bor ince ve eş eksenli taneciklerin oluşumunu destekler. Borun alüminyum malzeme üzerindeki bu tane inceltici etkisi nedeniyle günümüzde en çok tercih edilen tane inceltici (Al-Ti-B) olmasını sağlamıştır [2], [3].

Geleneksel döküm yöntemlerinde Al-Ti-B tane incelticileri; alüminyum, titanyum ve borun doğası gereği erime noktalarının farklı olması nedeni ile belirgin düzensizlikler ve topaklanma eğilimi gösterdiği bilinmektedir. Bu nedenle ikiz merdaneli döküm yöntemleri kullanılarak geliştirilmiş homojen yapı oluşumu ve hassas dağılım kontrolü elde etmek için uygun bir yol sunar ve böylece alüminyum alaşımlarının çeşitli endüstriyel ve teknolojik alanda uygulanabilirliğini arttırılabilir [4]–[7].

İkiz merdaneli döküm yöntemi, yüksek erime sıcaklıklarına olan ihtiyacı ortadan kaldırması, sürekli ve hızlı döküm yöntemine sahip olması nedeniyle geleneksel ergitme yöntemlerinden önemli ölçüde farklıdır. Geleneksel ergitme yöntemleri genellikle yüksek sıcaklıklar, daha uzun işlem süreleri ve kesintili toplu işlemler gerektirir [8]. İkiz merdaneli döküm yöntemi ise daha ince ve daha düzgün bir mikro yapı malzemelerin üretimine olanak sağlar, bu da mekanik özelliklerin ve yüzey kalitesinin iyileşmesine yol açar. Aynı zamanda enerji tüketimini azaltır ve alaşımın kirlenmesi riskini en aza indirir. Bu avantajlar ikiz merdaneli döküm yöntemini geleneksel yöntemlerden ayırarak alüminyumun alaşımlandırılması ve eritilmesi için daha verimli ve kaynakları koruyan bir alternatif haline getirmektedir [8], [9].

Bu çalışmada, alüminyum levhaların mekanik özelliklerini geliştirmek amacıyla iki farklı tane inceltici (Al-5Ti-0,2B ve Al-5Ti-1B) kullanılmış olup, üretim için hassas bir yöntem olan ikiz merdaneli döküm yöntemi uygulanmıştır. Çalışmada, elde edilen alüminyum alaşımının tane incelticilerinin metalografik, mekanik ve yüzey özelliklerine olan etkisi detaylı bir şekilde incelenmiştir. Geniş kapsamlı hedef olarak, Al-5Ti-0,2B ve Al-5Ti-1B tane incelticilerinin 1050 alüminyum alaşımı üzerindeki etkilerini gözlemleyerek, oluşturulan alaşımların mikroyapısı, mekanik özellikleri ve eloksallama işlemi üzerindeki etkilerini değerlendirilecektir.

2. Materyal ve Yöntem

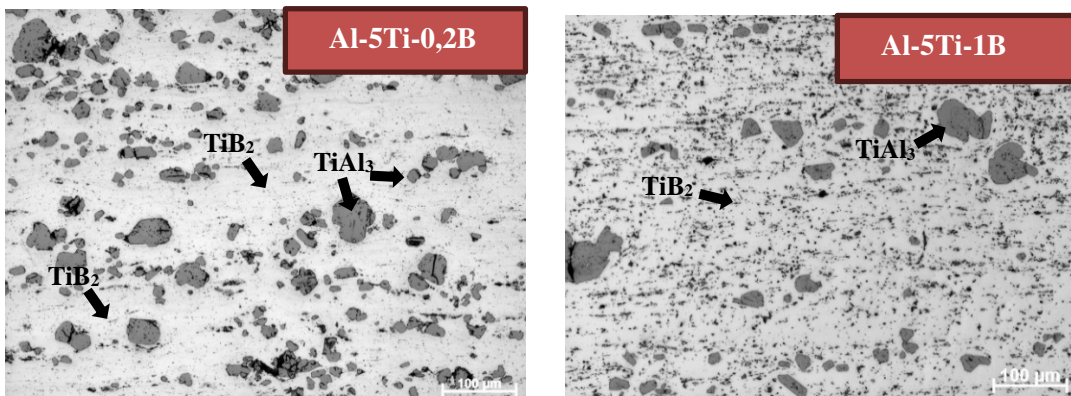
Bu çalışmada ikiz merdane döküm yöntemiyle üretilmiş AA1050 alaşımı kullanılmıştır. Aynı zamanda çalışmada Al-5Ti-0,2B ve Al-5Ti-1B olmak üzere iki farklı tane inceltici kullanılmıştır. Çalışma, 700-750 santigrat derece aralıktaki sıcaklıkta çalışan bir fırında kontrollü bir ergitme işlemine tabi tutulan %99,5 alüminyumdan oluşan alaşımı hazırlamak ile başlamıştır. Daha sonra erimiş alüminyum, tutma fırınlarına kesintisiz bir şekilde aktarılmıştır. Bu belirlenmiş tutma fırınlarından sıvılaştırılmış alüminyum, hassas bir şekilde belirlenmiş bir açıyla merdanelere giden

yolluklara doğru yönlendirilmiştir. Tane incelticinin (Al-5Ti-0,2 / Al-5Ti-1B) ilavesi, hidrojen giderimi ve mekanik filtrelemelerden geçen sıvı alüminyum yolluklar vasıtasıyla tundish sistemine aktarılıp tip vasıtasıyla merdanelere beslenmiştir. Merdaneler arasına transfer edilen sıvı alüminyum birbirine zıt halde hareket eden su soğutmalı merdane yüzeylerine temas eder etmez katılma meydana gelerek levha üretimi gerçekleşmiştir [8]–[11].

Üretilen levhaların kimyasal bileşimlerin tespiti için elementel analiz yapılmıştır. Elementel analiz Thermo Scientific marka ARL 4460 OES model optik emisyon spektrometre cihazı ile yapılmıştır. Daha sonra levhadan alınan numunelerin yüzey morfolojisi ve mikroyapı görüntüleri için ZEISS marka Scope.A1 model optik mikroskobu ve ZEISS marka EVO MA 15 model taramalı elektron mikroskobu (SEM) kullanılmıştır. Morfoloji açısından daha iyi görünüm elde edebilmek için zımparalama ve parlatma öncesi numuneler EpoFix Resin soğuk bakalite alınmış 24 saat kurumaya bırakılmıştır. Bakalite alınan numuneler Herzog marka freze makinesi ile frezelendikten sonra sırasıyla 500, 1200 ve 2400 SiC zımparalama kağıtları kullanılarak zımparalanmış, parlatma işlemi için de Struers marka Tegamin-30 cihaz üzerinde silika, kaydırıcı ve elmas süspansiyon kullanılarak parlatma işlemi gerçekleştirilmiştir. Struers marka elektrolitik dağlama cihazı ile tetreflora borik asit kullanılarak dağlama işlemi gerçekleştirilmiştir. Makro-sertlik ölçümü 62,5 kgf' luk kuvvet uygulanarak çapı 2,5 mm olan çelik bilye ile yapılmıştır. Mikro-sertlik ölçümü için Leica marka VMHT MOT model sertlik ölçüm cihazı kullanılmıştır. Mikrosertlik ölçümleri için hazırlanan kesit numunelerine 10 sn boyunca 50 gf yük uygulanmış olup, bu yük daha doğru sonuç elde edebilmek için numunenin 5 farklı bölgesine uygulanmış, ortalama sertlik değeri asıl sertlik değeri olarak belirlenmiştir. Çekme testi, ZwickRoell marka 50 kN kapasiteli cihaz kullanılarak gerçekleştirilmiştir. Numuneler için test hızı 10 mm/min olarak belirlenmiş olup, ölçme boyu 50 mm olarak ayarlanmıştır. Tüm numune ölçümleri DIN EN ISO 6892-1 test standartlarına uygun olarak 0° ve 90° yönlerinde her bir inceltici için ikişer adet olmak üzere toplamda dört numune üzerinde gerçekleştirilmiştir.

3. Bulgular ve Tartışmalar

Şekil 1'de alüminyum alaşımlarında kullanılan Al-5Ti-0,2 B ve Al-5Ti-1B tane incelticilerin ışık mikroskobu kesit mikroyapı görüntüleri yer almaktadır. İki tane inceltici arasında kompozisyondan da anlaşılacağı gibi içerdikleri bor elementi oranları farklıdır. Dolayısıyla mikroyapıda yer alan TiB₂ partikül miktarlarında resimlerden görüleceği üzere bazı farklılıklar göstermektedir. Al-5Ti-1B tane inceltici çok sayıda TiB₂ partikül içerirken Al-5Ti-0,2 B daha az sayıda TiB₂ içermekle birlikte TiAl₃ partiküllerinin nispeten çok sayıda ve büyük boyutlu olduğu anlaşılmaktadır. Tane inceltme mekanizmasında TiB₂ partiküllerinin heterojen çekirdeklenme mekanizması ile tane inceltmede daha etkin olduğu bilinmektedir. Çalışmada kullanılan Al-5Ti-1B tane incelticinin mikroyapıda diğer incelticiye göre çok daha küçük tane yapısı sağladığı Şekil 1'de açık bir şekilde görülmektedir [12], [13].



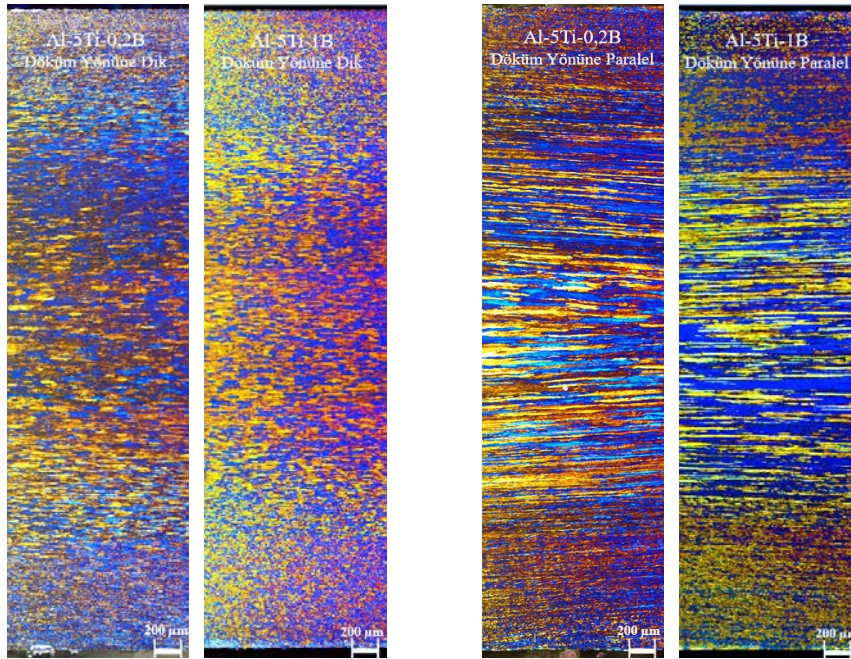
Şekil 1. Al-5Ti-0,2 B ve Al-5Ti-1B tane incelticilerin mikroyapısal analizi.

Alüminyum alaşımlarının kimyasal bileşimini tespit edebilmek için kapsamlı bir spektrometrik analiz yürütülmüştür. Ardından gelen kimyasal bileşim verileri dikkatli bir şekilde derlenmiş ve Tablo 1'de metodik olarak açıklanmıştır. Tablo 1.'de görüldüğü gibi Al- 5Ti-1B tane inceltici kullanılan alaşımın Al- 5Ti-0,2B tane inceltici kullanılan alaşıma göre içerdiği B miktarı yaklaşık 5 kat daha fazladır.

Tablo 1. Çalışmada kullanılan alaşımların kimyasal bileşimi.

İnceltici Türü	Al (%)	Ti (%)	B (%)
Al - 5 Ti - 0,2 B	99.552	0.023 -0.025	0.0005 -0.0010
Al - 5 Ti - 1 B	99.515	0.023 -0.025	0.0025 -0.0035

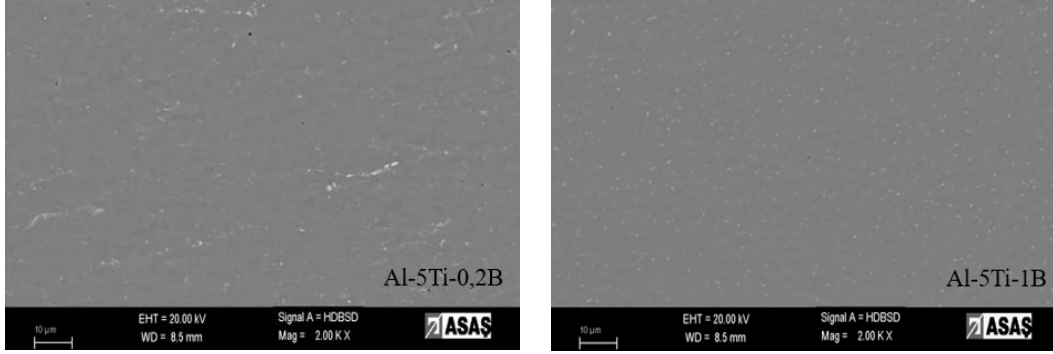
Al-5Ti-0,2B ve Al-5Ti-1B alaşımlarının mikro yapısal analizi ve tane büyüklüklerini karşılaştırmak amacıyla optik mikroskop kullanılarak mikroyapıları görüntülenmiştir (Şekil 2). İncelemelerde farklı tane inceltici kullanımı ile mikroyapıda daha ince ve eş eksenli yapı oluşumu elde edilmiştir. Bu tekdüzelik, tane dağılımı, metallar arası yapılar ve yüzey düzensizlikleri ile ilgili potansiyel sorunların önlenmesinde çok önemlidir. Böylesine homojen bir mikroyapı, olağanüstü yüzey kalitesi ve dayanıklılıkla karakterize edilen sağlam ürünlerin yaratılması için temel oluşturur [14], [15].



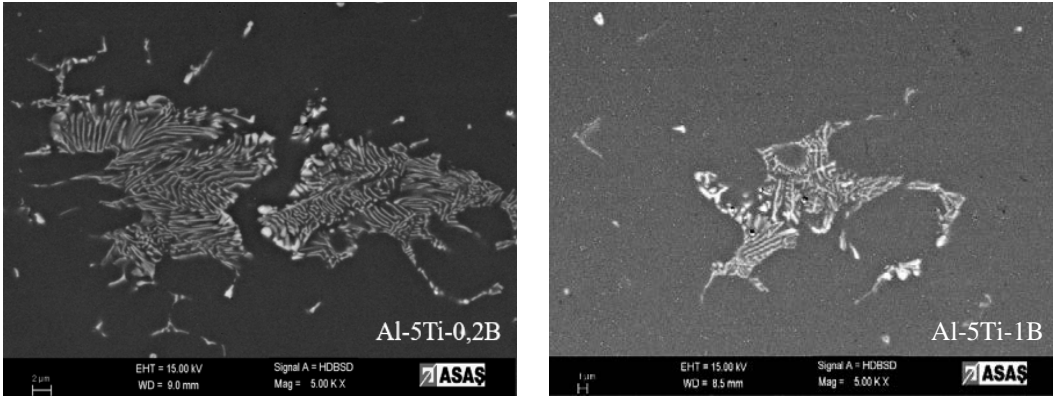
Şekil 2. Al-5Ti-0,2 B ve Al-5Ti-1B tane incelticilerden üretilmiş olan levhanın kesit mikroyapı görüntüleri.

Al-5Ti-0,2 B ve Al-5Ti-1B alaşımlarının yüzey ve intermetalik incelemeleri için SEM cihazı kullanılmıştır. İnceleme sonucunda; optik mikroskoptaki görüntüyü destekler nitelikte malzemenin homojen dağılımı net bir şekilde gözler önüne serilmiştir. Hem optik mikroskop görüntüleri hem de SEM görüntüleri Al-5Ti-1B alaşımının daha ince taneli olduğunu göstermektedir. Ayrıca Şekil 3.'de Al-5Ti-0,2B alaşımının içerisindeki beyaz olarak görülen intermetalik faz bölgelerinin homojen bir şekilde dağılmadığı ve lokal bölgelerde toplandığı görülmektedir. Böylece; Al-5Ti-1B alaşımının üstün çekirdeklenebilme yeteneği ile homojen bir dağılım sağlaması sayesinde intermetalik yapısı ve tane yapısındaki bu gelişim eloksallama gibi bu tür mikroyapısal etmenlere bağlı olan bir proses için olumlu bir etki yaratmaktadır. Şekil 4'te ayrıca levha kesit merkez hattında gözlemlenen merkez hattı segregasyonlarına ait SEM görüntüleri yer almaktadır. Resimde görülen merkez hattı segregasyonu

ötektikvari morfolojide Fe-Si-Al esaslı intermetalik fazlardan oluşmaktadır. Al-5Ti-1B tane incelticisinin katılma ve tane yapısında yarattığı etki nedeniyle merkez hattı segregasyonunun şiddetinin azaldığı görülmektedir. Daha etkin tane oluşumu ile matriste hapsolan elementler daha geç katılan merkez hattına difüze olamadan yapıda yer alıp merkez hattı segregasyonun şiddetinin azalmasına neden olmuştur [16], [17].

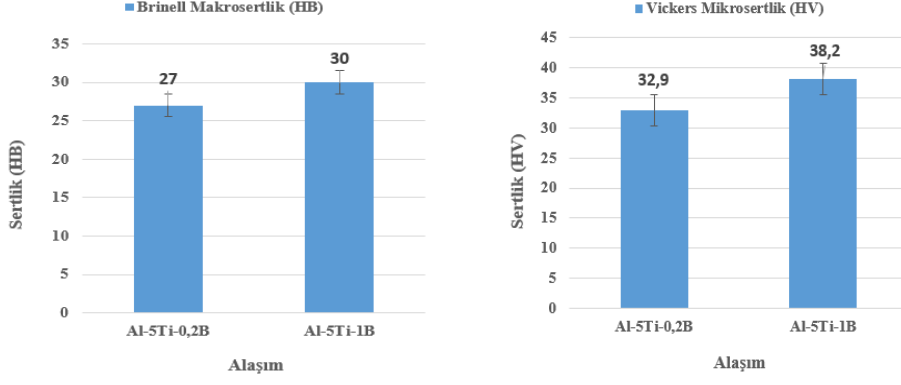


Şekil 3. Al-5Ti-0,2B ve Al-5Ti-1B tane incelticilerden üretilmiş olan levha kesit SEM görüntüleri.



Şekil 4. Al-5Ti-0,2B ve Al-5Ti-1B tane incelticilerden üretilmiş olan levha merkez hattı SEM görüntüleri.

Şekil 5'te iki alaşımın makro ve mikro sertlikleri karşılaştırılmıştır. Numunelerin yüzeyden Brinell makrosertlik ölçümleri yapıldığında; Al-5Ti-0,2B alaşımın ortalama yüzey sertlik değeri 27 HB iken, Al-5Ti-1B alaşımının ortalama yüzey sertliği 30 HB olarak ölçülmüştür. Numunelerin kesitten Vickers mikrosertlik ölçümleri yapıldığında ise Al-5Ti-0,2B alaşımın ortama sertlik değeri 32,9 HV iken, Al-5Ti-1B alaşımının ortalama sertliği 38,2 HV olarak ölçülmüştür. Al-5Ti-1B tane inceltici kullanılan alaşımda çekirdeklenmenin artması, tane yapısının homojen ve ince bir morfolojiye bürünmesi ile birlikte alaşımın sertliğinin artmasında çok büyük rol oynadığı görülmektedir [18]–[20]

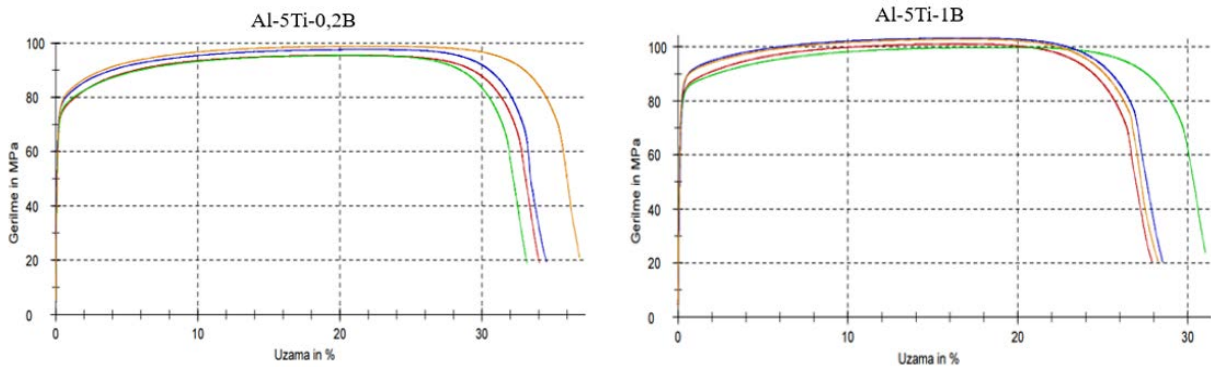


Şekil 5. Al-5Ti-0,2B ve Al-5Ti-1B tane incelticilerden üretilmiş olan levhaların makro-sertlik ve mikro-sertlik değerleri.

Al-5Ti-0,2B ve Al-5Ti-1B alaşımlarının çekme testi sonuçları Şekil 6'de verilmiştir. Bu alaşımların sırasıyla 0° ve 90° yönündeki akma ve çekme mukavemetleri Tablo 2'de verilmiştir. Al-5Ti-1B tane inceltici içeren alaşımların ince taneli olması, dolayısıyla daha fazla tane sınırı içermesi anlamına gelmektedir. Tane sınırları dislokasyon hareketini sınırladığı için daha fazla tane sınırı içeren alaşımların mukavemetinin ve sertliğinin daha yüksek olacağı anlamına gelmektedir. Hall-Petch bağıntısı da malzemelerin tane inceliği ile mukavemetleri arasındaki ilişkiyi açıklamaktadır [21], [22].

Tablo 2. Çekme testi sonuçları.

Numune Adı	Numune Yönü	Akma Dayanımı %0,2 (MPa)	Çekme Dayanımı (MPa)	Uzama A50 (%)
Al-5Ti-0,2B	0°	72	95	34
Al-5Ti-0,2B	0°	73	95	33,1
Al-5Ti-0,2B	90°	76	98	34,5
Al-5Ti-0,2B	90°	77	99	36,8
Al-5Ti-1B	0°	83	101	27,9
Al-5Ti-1B	0°	81	100	31
Al-5Ti-1B	90°	86	103	28,5
Al-5Ti-1B	90°	87	103	28,2



Şekil 6. Al-5Ti-0,2B ve Al-5Ti-1B tane incelticilerden üretilmiş olan levhaların çekme testi grafikleri.

Al-5Ti-0,2B ve Al-5Ti-1B alaşımları arasındaki temel fark borun (B) varlığında yatmaktadır. Al-5Ti-0,2B ve Al-5Ti-1B arasındaki farklar şunlardır:

- Mikroyapıya Etkisi: Al-5Ti-1B'un alüminyum alaşımına dahil edilmesi, alaşımın mikroyapısının homojenliğine yol açmıştır. Ayrıca; sertleşebilirliği geliştirmiş ve tane yapısını iyileştirerek intermetaliklerin oluşumu en aza indirilerek diğer mikroyapısal ve mekanik özellikleri de geliştirilmiştir. Al-5Ti-0,2B bor eksikliğinden dolayı aynı mikroyapısal değişiklikleri göstermemektedir.
- Mekanik Özellikler: Al-5Ti-1B 'de borun varlığı potansiyel olarak artan mukavemet ve sertlik gibi gelişmiş mekanik özelliklerle sonuçlanmıştır. Al-5Ti-0,2B ise bu özelliklerde aynı seviyede bir gelişme göstermemektedir.

4. Sonuçlar




- Bu çalışmada farklı bor içeriğine sahip Al-5Ti-0,2B ve Al-5Ti-1B tane incelticileri 1050 alüminyum alaşımı içerisine dahil edilerek başarılı bir şekilde üretilmiştir.
- SEM ve optik mikroskop görüntülerinden Al-5Ti-1B tane inceltici kullanılarak üretilen levha mikroyapısının ince taneli, homojen olduğu ve bunun yanında daha az şiddette merkez hattı segregasyonu oluşumuna katkı sağladığı belirlenmiştir.
- Daha yüksek bor içeriğine sahip Al-5Ti-1B tane inceltici içeren alaşımın diğer incelticiye göre AA 1050 alaşımı için daha fazla yeni çekirdekleyici bölgelerin oluşumu destekleyerek tane boyutunu incelttiği ve bu nedenle sertlik ve mukavemet özelliklerini daha fazla geliştirdiği kanıtlanmıştır.
- Al-5Ti-1B tane inceltici kullanımıyla tane yapısı ve intermetalik boyut ve dağılımlarında meydana gelen gelişimler eloksallama yüzey işleminin istenen yüzey kalitede elde edilmesine olanak sağlamıştır.

Kaynaklar

- [1] E. Bayseçkin, "Sürekli döküm yöntemiyle alüminyum levhalarda döküm ve homojenleştirme sürecinde mikro yapısal değişimin incelenmesi.," 2002.
- [2] M. B. YAMAN, E. KOCAMAN, and B. AVAR, "Al7075 Alaşımına İlave Edilen Al-5Ti-1B Tane İncelticinin Yaşlanma, Mikroyapı, Sertlik ve Korozif Özellikleri Üzerindeki Etkisi," *Gazi Üniversitesi Fen Bilimleri Dergisi Part C: Tasarım ve Teknoloji*, vol. 10, no. 4, pp. 870–883, Dec. 2022, doi: 10.29109/GUJSC.1165103.
- [3] M. Çolak *et al.*, "ALÜMİNYUM DÖKÜMLERİNDE TANE İNCELTME," *Sakarya University Journal of Science*, vol. 13, no. 1, pp. 11–17, Jun. 2009, doi: 10.16984/SAUFBED.70075.
- [4] F. XIAO *et al.*, "Effect of trace boron on grain refinement of commercially pure aluminum by Al-5Ti-1B," *Transactions of Nonferrous Metals Society of China (English Edition)*, vol. 32, no. 4, pp. 1061–1069, Apr. 2022, doi: 10.1016/S1003-6326(22)65855-2.
- [5] A. Paşa Hekimoğlu, Y. E. Turan, İ. İ. İsmailoğlu, E. Akyol, and E. Şen, "Effect of grain refinement with boron on the microstructure and mechanical properties of Al-30Zn alloy," *Journal of the Faculty of Engineering and Architecture of Gazi University*, vol. 34, pp. 523–534, 2019, doi: 10.17341/gazimmfd.416512.
- [6] E. Kocaman and S. Şirin, "Effect of Al5Ti1B Grain Refiner and Al10Sr Modifier on Mechanical Properties and Corrosion Behavior of A360 Alloy," *International Journal of Automotive Science And Technology*, vol. 7, no. 1, pp. 30–36, Apr. 2023, doi: 10.30939/IJASTECH..1237345.
- [7] L. Lu, M. O. Lai, and H. Y. Wang, "Synthesis of titanium diboride TiB2 and Ti-Al-B metal matrix composites," *J Mater Sci*, vol. 35, no. 1, pp. 241–248, 2000, doi: 10.1023/A:1004789910279/METRICS.

- [8] © Metallurgical and M. Industry, “Twin-roll Casting of High-strength Age-hardened Aluminium Alloys,” vol. 3, no. 7, 2011.
- [9] F. Karakoyun, “THE EFFECTS OF ALLOYING ELEMENTS ON THE MICROSTRUCTURE AND ANNEALING BEHAVIOR OF THE TWIN-ROLL CAST AA1050 STRIP,” 2004.
- [10] O. Mutlu, “AA1050 ALÜMİNYUMUN HACİMSSEL VE YÜZEYSSEL AŞIRI PLASTİK DEFORMASYON YÖNTEMLERİ İLE MEKANİK ÖZELLİKLERİNİN İYİLEŞTİRİLMESİ 2019 YÜKSEK LİSANS TEZİ MAKİNA MÜHENDİSLİĞİ”.
- [11] A. Kadri Can, “The Effects of Solidification Conditions on The Formability of The Twin-Roll Cast AA1050 Strip “,” *Mechanical Engineering Thesis , Boğaziçi University , Istanbul , Turkey*, 2007.
- [12] İ. ARSLAN, E. GAVGALI, and M. ÇOLAK, “Kum Kalıba Dökülen Farklı Alüminyum Alaşımlarının Dökümünde AL5Ti1B ve AL10SR İlavesinin Mikroyapı Özelliklere Etkisinin İncelenmesi,” *Akademik Platform Mühendislik ve Fen Bilimleri Dergisi*, vol. 7, no. 2, pp. 237–244, May 2019, doi: 10.21541/APJES.424920.
- [13] Hu, M., Wang, F., Jiang, B., Wang, H., Liu, Y., & Ji, Z. (2022). Fabrication of Al–Ti–B Grain Refiner Using Machining Ti Chips, Reaction Mechanisms and Grain Refinement Performance in Pure Al. *Metals and Materials International*, 1-9, 2021, doi: 10.1007/s12540-021-01011-9
- [14] S. Lin, C. Aliravci, and M. O. Pekguleryuz, “Hot-Tear Susceptibility of Aluminum Wrought Alloys and the Effect of Grain Refining,” *Metallurgical and Materials Transactions A*, vol. 5, no. 38, pp. 1056–1068, 2007, doi: 10.1007/S11661-007-9132-7.
- [15] Y. Luo *et al.*, “Effect of Warm Rolling on the Grain-Refining Performance of Al-5Ti-1B Grain Refiner in Al,” *JOM*, vol. 74, no. 3, pp. 1210–1217, Mar. 2022, doi: 10.1007/S11837-021-05137-4.
- [16] S. Basak, P. Biswas, S. Patra, H. Roy, and M. K. Mondal, “Effect of TiB₂ and Al₃Ti on the microstructure, mechanical properties and fracture behaviour of near eutectic Al-12.6Si alloy,” *International Journal of Minerals, Metallurgy and Materials*, vol. 28, no. 7, pp. 1174–1185, Jul. 2021, doi: 10.1007/S12613-020-2070-8/METRICS.
- [17] H. Ashassi-Sorkhabi, M. Moradi-Haghighi, and M. G. Hosseini, “Effect of rare earth (Ce, La) compounds in the electroless bath on the plating rate, bath stability and microstructure of the nickel-phosphorus deposits,” *Surf Coat Technol*, vol. 202, no. 9, pp. 1615–1620, Feb. 2008, doi: 10.1016/j.surfcoat.2007.07.019.
- [18] R. Can *et al.*, “Toz Metalurjisi Yöntemi ile Tane İnceltici Üretimi ve Döküm Performansının İncelenmesi,” *Uluslararası Mühendislik Araştırma ve Geliştirme Dergisi*, vol. 15, no. 1, pp. 151–163, Jan. 2023, doi: 10.29137/UMAGD.1167854.
- [19] Izcankurtaran, D., Tunca, B., & Karatay, G. (2021). Investigation of the effect of grain refinement on the mechanical properties of 6082 aluminium alloy. *Open Journal of Applied Sciences*, 11(6), pp. 699-706, Jun. 2021, doi: 10.4236/ojapps.2021.116051
- [20] A. B. Pattnaik, S. Das, B. B. Jha, and N. Prasanth, “Effect of Al–5Ti–1B grain refiner on the microstructure, mechanical properties and acoustic emission characteristics of Al5052 aluminium alloy,” *Journal of Materials Research and Technology*, vol. 4, no. 2, pp. 171–179, Apr. 2015, doi: 10.1016/J.JMRT.2014.10.017.
- [21] Y. Wen, Y. Wu, Y. Wu, T. Gao, Z. Wei, and X. Liu, “Effect of Al-5Ti-0.25C-0.25B and Al-5Ti-1B Master Alloys on the Microstructure and Mechanical Properties of Al-9.5Si-1.5Cu-0.8Mn-0.6Mg Alloy,” *Materials 2023, Vol. 16, Page 1246*, vol. 16, no. 3, pp. 1246, Feb. 2023, doi: 10.3390/MA16031246.
- [22] M. Alipour, “The Comparison of Effects of Ultrasonic Treatment, SIMA Process and Al-5Ti-1B Grain Refiner on the Microstructure and Mechanical Properties of Al–15%Mg₂Si in-situ Composite,” *Iranian Journal of Materials Science and Engineering*, vol. 20, no. 1, pp. 97–114, Mar. 2023, doi: 10.22068/IJMSE.2957.

Investigation of the Effect of Huntit Filler on Flame Retardancy and Mechanical Properties of Silicone Rubber-based Materials in Cable Applications

*^{1,2} Halil Can Uğraşkan  0009-0002-6410-4995, ^{1,2} Fatma Sevde Duman  0009-0007-5827-2120, ² Serkan Emik  0000-0002-6005-9704

¹ 2M Kablo San. Tic. A.Ş., Department of R&D Center, Tekirdağ, Turkey.

² Istanbul University-Cerrahpaşa, Chemical Engineering Depart., Istanbul, Turkey.

* Corresponding author, e-mail: halilcanugraskan5@gmail.com

Submission Date: 04.12.2023

Acceptation Date: 18.12.2023

Abstract

Silicone rubber is an organic/inorganic hybrid macromolecular polymer with properties such as fire resistance, strength, flexibility, chemical resistance, thermal stability, hydrophobicity, dielectric characteristics, resistance to environmental conditions, and biocompatibility. It is an elastomer and exhibits high-performance characteristics compared to most materials in its class. Its current properties and the relative ease of enhancing its characteristics have significantly increased the industrial utilization of silicone rubber. Due to its mineral structure, silicone rubber is frequently used as an insulating material to ensure circuit integrity in the production of fire-resistant cables. It exhibits low smoke zero halogen (LSZH) characteristics, with low level release of toxic gases as a result of combustion reactions. In this study, silicone rubber compounds including a natural mineral Huntite with improved fire-resistant properties compared to standard silicone materials suitable for cable production were prepared. After cable production the fire performance properties alongside the physico-mechanical characteristics of the final products were examined. To determine the flame retardancy of the material, limiting oxygen index (LOI%) and fire performance tests were performed according to the ISO 4589-2 and BS 6387 standards, respectively. The results show that Huntite is a suitable alternative material to improve silicone materials' flame resistance.

Keywords: Silicone rubber, Huntite-Hydromagnesite, Fire-retardant, Cable, Fire tests

Huntit Dolgusunun Silikon Kauçuk Üzerinde Alev Geciktirici ve Mekanik Özelliklerine Etkisinin Kablo Uygulamalarında İncelenmesi

Öz

Silikon kauçuk, yangına dayanıklılık, mekanik dayanıklılık, esneklik, kimyasal direnç, termal stabilite, hidrofobiklik, dielektrik karakteristikleri, çevresel koşullara karşı direnç ve biyolojik uyumluluk gibi özelliklere sahip organik/inorganik hibrid bir makromoleküler polimerdir. Elastomer sınıfındaki çoğu malzeme ile karşılaştırıldığında yüksek performans özellikleri sergiler. Sahip olduğu bu özellikler ve bu özelliklerin geliştirilmesinin göreceli kolay olması, silikon kauçuğun sanayide kullanımını önemli ölçüde artırmaktadır. Mineral yapısı nedeniyle silikon kauçuk yangına dayanıklı kabloların üretiminde devre bütünlüğünü sağlamak için bir yalıtkan malzeme olarak sıkça kullanılmaktadır. Yanma reaksiyonları sonucunda toksik gazların düşük seviyede salınımı ile düşük duman ve sıfır halojen (LSZH) özelliklerine sahiptir. Bu çalışmada, kablo üretimine uygun standart silikon malzemelere göre yangına dayanıklılık özellikleri geliştirilmiş, doğal bir mineral olan Huntit içeren silikon kauçuk bileşikleri hazırlanmıştır. Kablo üretiminden sonra nihai ürünün fiziko-mekanik özelliklerinin yanı sıra yangın performans özellikleri de incelenmiştir. Kabloların alev geciktirici özelliklerini belirlemek için ISO 4589-2 ve BS 6387 standartlarına göre sırasıyla sınırlı oksijen indeksi (LOI%) ve yangın performans testleri gerçekleştirilmiştir. Sonuçlar Huntitin silikon malzemelerin alev direncini arttırmak için uygun bir alternatif malzeme olduğunu göstermektedir.

Anahtar kelimeler: Silikon kauçuk, Huntit-Hidromagnezit, Alev geciktirici, Kablo, Alev testleri

¹ Corresponding author:
E-mail: halilcanugraskan5@gmail.com

1. Introduction

Silicone rubber (SR) is a semi-organic and semi-inorganic material with low heat release rate, low total heat release, and low fire index. [1-6] At the same time, SR has excellent thermal stability, which is transformed into a continuous, oxidation-resistant, insulating network-like silica ash covering the surface after burning, [7] effectively preventing further ablation. Its existing properties and the relative ease of property improvement significantly increase the use of silicone rubber in industry. Which is that silicone rubber is an excellent material to ensure the circuit integrity. However, its own flame retardancy performance is not enough to meet the requirements of products, such as fire door and fireproof cable material. [8,9]

In fire-resistant cable applications, the performance of SR material is insufficient to pass the tests required to meet standards such as BS 6387 protocols C, W, and Z. Therefore, in fire-resistant cable applications, the selection of materials and their compounding is crucial.

Nowadays, the most widely used groups of mineral fire retardants are metal hydroxides such as Aluminum hydroxide (ATH) and Magnesium Hydroxide (MDH). In addition, silicone dioxide and calcium carbonate are the most widely used groups of cost-effective mineral fillers in industrial applications.

In silicone rubber compounding, inorganic reinforcement agents, especially silicon dioxide, are commonly used to modify mechanical properties such as tensile strength, elongation, and hardness according to the filler's particle size. Since these fillers has inorganic structure, they also improve the char forming properties, resulting in improved flame-retardant properties. But the main utilization of reinforcement agents is cost reduction.

Metal hydroxides act as fire retardants by releasing water vapor through endothermic decomposition leaving a thermally stable inorganic residue. When used as a filler in polymer composites, they dilute the combustible polymer decomposition products with water, cooling the condensed phase through the endothermic dehydration.

Nowadays, the use of mineral rocks as flame retardant fillers in industrial applications is becoming widespread. Considering the literature studies, grinding them to appropriate sizes, causes both flame retardancy as well as cost reduction. There are studies in the literature on the utilization of Huntite-Hydromagnesite among these filler materials such as Aluminum hydroxide (ATH) , Magnesium hydroxide (MH), Zinc Borate (ZB), Colemanite (C). [10-14]

Huntite, with the formula $Mg_3Ca(CO_3)_4$, is a rock-type carbonate compound found mixed with Hydromagnesite in nature and can be produced in desired particle sizes with modern grinding technology. It decomposes by an endothermic reaction similar to ATH and MDH. Decomposition begins with the separation of chemically bound H_2O at temperatures above $240^\circ C$, and forms char in the physically stable Mg and Ca oxide structure with the separation of CO_2 at high temperatures ($450-800^\circ C$) [15].

Since the discovery of natural Huntite-Hydromagnesite deposits in late 1980's, there has been considerable number of works published regarding the structure [16-21] and thermal decomposition [22-37] of Huntite-Hydromagnesite materials. Due to its two-stage decomposition using Huntite-Hydromagnesite mineral instead of Quartz in silicone rubber compound is promising for fire retardancy applications.

In this study, it was aimed to examine the use of natural mineral filler Huntite instead of quartz, which is widely used in silicone rubber compositions, in terms of both mechanical and fireproof properties. For this purpose, mechanical and fire-retardant properties of Silicone Rubber/Huntite

composites were investigated by comparing them with a standard Silicone/Quartz composite. By subjecting the cables produced by the standard extrusion method to the relevant international fire tests, the effect of Huntite mineral as a fire-retardant material for silicone compounds for cable production applications has been scientifically investigated.

2. Materials and Methods

2.1. Materials

Two different peroxide curable high-consistency rubber (HCR) silicone rubber, commercial name Elastosil R 401/55 S and Elastosil R 500/60 OH was purchased from Wacker Chemie AG, (Munich, Germany). Natural Huntite-Hydromagnesite mineral was purchased from Minelco Ltd., (İzmir, Turkey). The curing agent, di(2,4-dichlorobenzoyl) peroxide was purchased from Akzo Nobel GmbH, (Amsterdam, The Netherlands) and the coloring blue pigment was purchased from Rockwood Pigments (Kingsgrove, England). All materials were used as received.

2.2. Sample Preparation

Silicone rubber composites were prepared using two roll-mill operating at room temperature according to formulations given in Table 1. The silicone rubbers were initially softened, after Huntite-Hydromagnesite mineral were introduced as fillers. The Rubber and filler thoroughly mixed until a visually homogeneous mixture was achieved. After 25 minutes of mixing, a curing agent, DCBP, was added to the system. The total mixing time extended to approximately 30 minutes. Following the compounding process, the silicone rubbers were allowed to condition for 16 hours. Subsequently, the silicone rubber formulations were extruded onto copper wire with a 1.5 mm² surface area using an extruder with 90 mm screw diameter to form the cores of the selected LIHH 2x1.5mm² control cable for this study. For a reference sample SR/Quartz composite has been chosen. All of these production steps applied as same for the sample 2M30.

Table 1. Formulations of Silicone rubber composites

Composition (phr)	Compound Code			
	2M204	2M205	2M206	2M30
Silicone Rubber /1	50,00	50,00	50,00	50,00
Silicone Rubber /2	50,00	50,00	50,00	50,00
Huntite-Hydromagnesite	20,00	25,00	30,00	-
Quartz	-	-	-	30,00
Curing agent	1,35	1,35	1,35	1,35
Coloring pigment	0,35	0,35	0,35	0,35

The general schematic view of the continuous extrusion process used in the study, which includes (i) extruding SR on wire, (ii) passing the covered wire through the heat-shocking units located downstream of the extrusion line, (iii) the vulcanization process by passing through a hot air-flowing heat tunnel is given in Figure 1.

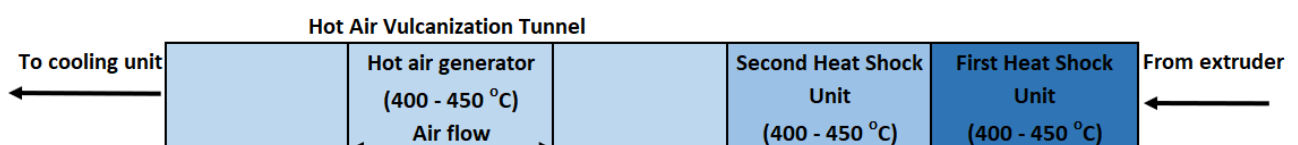


Figure 1: General schematic view of the extrusion process

As seen in Figure 2, the selected LIHH type cable's structure consists of multiple layers: While stranding the cable cores (produced by SR extrusion process) to form the appropriate structure, they are stranded with a layer of fiberglass tape. Finally, to give the cable its final form, a HFFR material is extruded as outer sheath.

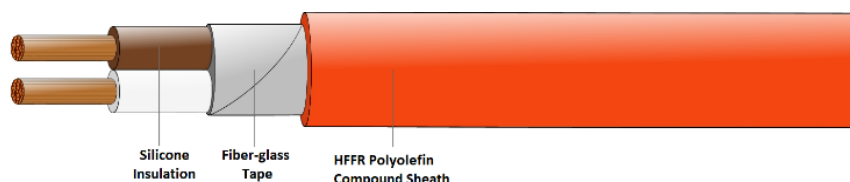


Figure 2: LIHH type cable's structure

2.3. Characterization Methods

Rheological analysis performed by a moving die rheometer MDR (Gotech M-3999AU). Analysis carried out at 120°C for 5 min. The torque value was monitored as a function of time. In rheological analysis, standard curing parameters:

ML, minimum torque – A measure of the viscosity of the uncured compound.

MH, maximum torque – A measure of cure state. With some compounds, maximum torque can be related to vulcanizate modulus and hardness.

ts₂ – time for torque to increase 0.2N.m or above ML – a measure of scorch time or processing safety.

t₁₀, t₅₀, t₉₀ – time to reach 50% or 90% of maximum torque development, calculated as time to 0.5 MH or 0.9 MH – a measure of cure rate or an estimate of cure time at the test temperature.

were investigated.

Tensile strength and elongation measurements were performed using Universal Testing Machine (Zwick model Z005) at room temperature. Tensile tests conducted on dumbbell shaped samples (125x75x3.0 mm³) at a speed of 50 mm/min according to the standard IEC/EN 60801. Tensile strength, percentage elongation at break and modulus values were recorded. All the results were calculated with an average value of five samples with standard deviations.

The material's hardness was determined utilizing a digital Shore A durometer (ZwickRoell 3130). For this purpose, test plates with dimensions of 10x10x0.3 cm³ were prepared using a hot press (Marestek M-gps-01) at 180°C for 6 minutes under a pressure of 150 MPa with SR materials.

LOI values were measured by Oxygen Index analyzer (Mares) on test bars of size 130x6.5x3.2 mm³, according to the ISO4589-2 determination of oxygen index test standard.

The fire performance of silicone materials was evaluated on the final product through the application of C-W and Z tests in accordance with the BS 6387 standard, PH120 test according to EN 50200 standard and FE 180 test according to IEC 60331-21/23. One of the important applications of these composites is their behavior in fire simulation. Protocol C test involves the application of only flame onto the cable, while Protocol W test simulates the scenario where fire extinguishing systems apply water jets onto the cable while flames are present during a fire. On the other hand, Protocol Z test is designed to assess the impact of falling objects onto the cable or the system containing the cable during a fire. PH 120 test involves mounting the cable in a U-shape on a vertical wall and applying force during the free-fall motion of a cylindrical rod with a mass of 25 kg onto the wall where the cable is mounted, under the flame at a temperature of 830°C, to assess the circuit integrity. In the FE 180 test, the cable must operate without compromising circuit integrity for a minimum of

180 minutes under a flame at a temperature of at least 750°C. These fire tests aim to assess situations that could compromise circuit integrity in a real fire scenario.

According to the BS 6387 standard, in these tests, the cable is installed on the test apparatus, and the declared voltage is applied to the conductors. The cable is then subjected to a flame at $950 \pm 40^\circ\text{C}$ for Protocol C, $650 \pm 40^\circ\text{C}$ for Protocol W, and $950 \pm 40^\circ\text{C}$ for Protocol Z. In all these tests cable must maintain its electrical continuity.

According to BS 6387 standard, in C fire test protocol, flame at a temperature of $950 \pm 40^\circ\text{C}$ is applied to the cable, which is mounted parallel to the flame source burner with a distance of 75 mm. The cable tested for 180 minutes must maintain its electrical continuity.

According to BS 6387 standard, the W fire test protocol involves a total duration of 30 minutes. Starting from the 15th minute of the test, the cable is subjected to water spray with a rate of $0.25 \text{ L/m}^2/\text{s}$. The cable must maintain its electrical continuity for an additional 30 minutes under the water spray. In accordance with the BS 6387 standard, the Z protocol apparatus incorporates a rod weighing 25 kg. At 30-second intervals, this rod undergoes free fall motion, inducing vibrations on the wall to which the cable is affixed.

Aging tests were conducted on the insulation part of the cores. The copper wire separated from the silicone insulation without causing damage to the material. The test was carried out inside an oven at a temperature of 200°C for a duration of 10 days. Tensile measurements were performed after 16 hours of conditioning, and the percentage changes were recorded.

3. Results and Discussions

3.1. Rheological Behavior of Composites

The Elastosil R 401/55 S and Elastosil R 500/60 OH HCRs are noted for their easy pigmentation, good flexibility, good processing characteristics, and mechanical properties. After preparing the silicon rubber compounds, firstly, the curing characteristics of these compounds were investigated. For this purpose, the torque versus time curves were obtained in a moving die rheometer for 5 minutes at 120°C under $1.67 \text{ Hz} \pm 0.01$ oscillating frequency. As seen in Table 2 and Figure 3, while the addition of filler did not affect the T_{s2} , T_{10} , and T_{50} and slightly increased T_{90} values (that is, it did not cause any significant change in the vulcanization process), it caused an expected increase in the measured maximum torque value. The results indicated that the all-silicone rubber compounds have good processability, and can be easily cured by extrusion process.

Table 2: Vulcanization parameters of the composites

	MH	ML	T_{s2}	T_{10}	T_{50}	T_{90}
	(dN-m)	(dN-m)	(m:s)	(m:s)	(m:s)	(m:s)
2M204	15,889	4,521	00:22	00:21	00:28	00:49
2M205	15,027	3,66	00:22	00:21	00:28	00:47
2M206	16,821	4,716	00:22	00:21	00:28	00:50
2M30	18,924	6,314	00:22	00:21	00:28	00:53

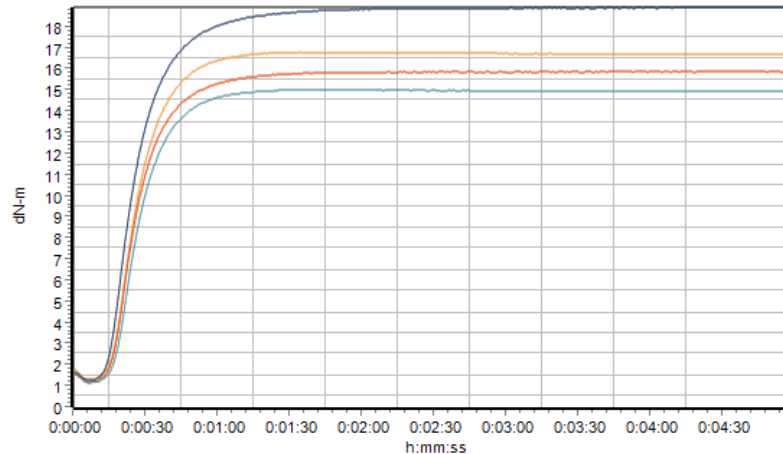


Figure 3: Rheological analysis of the composites

3.2. Mechanical Properties

The values of all mechanical parameters did not change significantly (Table 3) compared to 2M30 sample. This indicates that the Huntite-Hydromagnesite mineral allows the use of this compound as insulation for a wire, which is a crucial parameter for cable standards. Conversely, addition of mineral filler has resulted in an improvement in the Shore A hardness value (Table 4).

Table 3: Mechanical test results according to IEC/EN 60801

Tensile Strength Composition (phr)	Sample designation			
	2M 204	2M205	2M206	2M30
Dumbbell	7,72	8,51	7,34	8,45
Standard Deviation	0,30	0,39	0,14	0,45
Core insulation	6,44	7,42	7,78	8,18
Standard Deviation	0,26	0,30	0,17	0,21

Elongation Composition (phr)	Sample designation			
	2M 204	2M205	2M206	2M30
Dumbbell	380,90	443,13	380,21	384,92
Standard Deviation	22,40	45,91	19,50	23,73
Core insulation	459,50	344,60	368,71	346,90
Standard Deviation	36,54	38,22	26,90	32,48

3.3. Aging Properties

Cables are electrical equipment that need to be used for a long time, therefore, it is necessary to examine the aging characteristics of cable insulation materials through thermal aging tests. The compliance of cables with the IEC/EN 60811-401 and IEC/EN 60811-501 standards has been assessed through thermal aging tests, and the effect of Huntit-Hydromagnesite mineral on thermal aging has been investigated. As seen in Table 4, the use of filling material at a rate of 30 phr indicates that the material does not meet the specified standards. It has been determined that the most optimal level for the usage rate of the filling material, based on aging characteristics, is 25 phr.

Table 4: Thermal aging test results according to IEC/EN 60811-401 and IEC/EN 60811-501

Compound	Tensile strength* (N/mm ²)	Elongation* (%)
2M204	4,58	166,254
2M205	4,49	140,42
2M206	2,16	104,37
2M30	5,68	147,7

*: Standard values for Tensile Strength= 4 N/mm² and Elongation= 120%

3.4. Flame Retardancy Properties

Table 5 and 6 present the results of BS 6387, EN50200 and IEC 60331-21/23 fire tests and LOI test.

Table 5: Results of Flame Tests

Insulation Material	FE 180	PH 30	BS 6387 C	BS 6387 W	BS 6387 Z
2M204	✓	✓	✓	X	✓
2M205	✓	✓	✓	X	✓
2M206	✓	✓	✓	X	✓
2M30	✓	✓	✓	X	✓

Table 6: Results of LOI Test

Compound	2M204	2M205	2M206	2M30
LOI (%)	28	29	30	29

As seen in the table 5 and table 6, all samples exhibit exceptional fire resistance. Addition of Huntite-Hydromagnesite at 20, 25 and 30 phr also improved char formation significantly.

The two-stage degradation mechanism of Huntite-Hydromagnesite mineral delays the spread of flames, while the resulting fused silica structure, along with the ash-retaining effect of the fiberglass tape, forms a protective layer on the copper surface. This condition ensures the circuit integrity of the cable even under the most challenging conditions. This char formation helps the cable structure pass fire tests except BS 6387 W. It is concluded that the main reason why no formulation can pass the BS 6387 W test is that the water spray in this test is a sign that the char formed as a result of combustion has a porous structure. CO₂ and water formed during the thermal decomposition of huntite cause the resulting char to become porous. It is thought that with the extra additives added to the formulations, products that can successfully pass the BS 6387 W test can be produced due to a less porous and more durable char formation, in other words ceramified char structures. Nevertheless, since all cable structures have high LOI values and pass fire tests except BS 6387 W, it can be easily said that huntite is a highly effective mineral filler in the production of fire-resistant silicone cables.

4. Conclusions

Despite obtaining positive results in fire tests conducted according to specified standards for all samples, the sample incorporating 30 phr Huntite filler yielded unfavorable outcomes in aging tests conducted within the ambit of IEC/EN 60811-401 and IEC/EN 60811-501.

Notwithstanding the affirmative outcomes in BS 6387 C-Z tests and IEC 60331-21/23 FE 180 tests for all tested compounds, the fire test performance of the compounds fell short of meeting the terms of BS 6387 W. It is discerned that the final products lack resistance to the water factor in the BS 6387 W test.

In light of these findings, the optimal ratio of Huntite-Hydromagnesite filler for cable applications appears to be 25 phr. The cost-effectiveness relative to the base compound has facilitated

the simultaneous enhancement of both properties and cost in the final product by augmenting the quantity of Huntite material.

Peer-review: Externally peer - reviewed.

Author contributions: Concept – H.C.U., S.E.; Data Collection &/or Processing – F.S.D.; Literature Search - H.C.U., S.E.; Writing - H.C.U and F.S.D. All authors discussed the results and commented on the manuscript.

Conflict of Interest: This paper has been presented at the UKMK-15 (15th National Chemical Engineering Congress) held in Çanakkale (Turkey), September 4-7, 2023.)

Financial Disclosure: This study has been supported by 2M Kablo R&D Center, AGM22C010523 “Yangın güvenlik kablolarında kullanılan silikon malzemesinin üretiminde kullanılan kauçuk ve katkı malzemelerinin etkisinin incelenmesi ve reçete optimizasyonu”

References

- [1] Mansouri J, Wood CA, Roberts K, Cheng YB, Burford RP. Investigation of the ceramifying process of modified silicone-silicate compositions. *J Mater Sci.* 2007;42(15):6046-6055.
- [2] Radhakrishnan TS. New method for evaluation of kinetic parameters and mechanism of degradation from pyrolysis-GC studies: thermal degradation of polydimethylsiloxanes. *J Appl Polym Sci.* 1999;73(3): 441-450.
- [3] Hamdani S, Longuet C, Perrin D, Lopez-cuesta JM, Ganachaud F. Flame retardancy of silicone-based materials. *Polym Degrad Stab.* 2009;94(4):465-495.
- [4] Buch R. Rates of heat release and related fire parameters for silicones. *Fire Saf J.* 1991;17(1):1-12.
- [5] Belot V, Corriu RJP, Leclercq D, et al. Thermal redistribution reactions in crosslinked polysiloxanes. *J Polym Sci Part A Polym Chem.* 2010;30 (4):613-623.
- [6] Hshieh FY, Buch RR. Controlled-atmosphere cone calorimeter studies of silicones. *Fire Mater.* 1997;21(6):265-270.
- [8] Yue, Y., Zhang, H., Zhang, Z., & Chen, Y. (2013). Polymer–filler interaction of fumed silica filled polydimethylsiloxane investigated by bound rubber. *Composites Science and Technology*, 86, 1–8. <https://doi.org/10.1016/j.compscitech.2013.06.019>
- [9] Li, Z., Liang, W., Shan, Y., Wang, X., Yang, K., & Cui, Y. (2019). Study of flame-retarded silicone rubber with ceramifiable property. *Fire and Materials*, 44(4), 487–496. <https://doi.org/10.1002/fam.2802>
- [7] Mei N. Advance in the research and application of flame-retardant and fireproof silicone rubber. *New Chem Mater.* 2008;36(2):8-9.
- [10] Savas, L. A., Deniz, T. K., Tayfun, U., & Dogan, M. (2017). Effect of microcapsulated red phosphorus on flame retardant, thermal and mechanical properties of thermoplastic polyurethane composites filled with huntite&hydromagnesite mineral. *Polymer Degradation and Stability*, 135, 121–129. <https://doi.org/10.1016/j.polymdegradstab.2016.12.001>
- [11] Basfar, A. A., & Bae, H. J. (2009). Influence of Magnesium Hydroxide and Huntite Hydromagnesite on Mechanical Properties of Ethylene Vinyl Acetate Compounds Cross-linked by

DiCumyl Peroxide and Ionizing Radiation. *Journal of Fire Sciences*, 28(2), 161–180. <https://doi.org/10.1177/0734904109340765>

[12] Cusack, P. A., & Hornsby, P. R. (1999). Zinc stannate-coated fillers: Novel flame retardants and smoke suppressants for polymeric materials. *Journal of Vinyl and Additive Technology*, 5(1), 21-30.

[13] Wilkie, C. A., & Grand, A. F. (2000). *Fire Retardancy of Polymeric Materials*. Taylor & Francis Group, (Wilkie & Grand, 2000, p. 285-343)

[14] Dogan, M., Dogan, S. D., Savas, L. A., Ozcelik, G., & Tayfun, U. (2021). Flame retardant effect of boron compounds in polymeric materials. *Composites Part B: Engineering*, 222, 109088. <https://doi.org/10.1016/j.compositesb.2021.109088>

[15] Yücel Bayram, M., Gül Özgen, (2017) *Dünyada ve Türkiye’de Huntit Maden Tetkik ve Arama Müdürlüğü; Maden Serisi 4*. <https://www.mta.gov.tr/v3.0/sayfalar/bilgi-merkezi/maden-serisi/Huntit.pdf> Last visited: 04.12.2023

[16] Akao, M., & Iwai, S. (1977). The hydrogen bonding of hydromagnesite. *Acta Crystallographica Section B Structural Crystallography and Crystal Chemistry*, 33(4), 1273–1275. <https://doi.org/10.1107/s0567740877005834>

[17] Akao, M., Marumo, F., & Iwai, S. (1974). The crystal structure of hydromagnesite. *Acta Crystallographica Section B Structural Crystallography and Crystal Chemistry*, 30(11), 2670–2672. <https://doi.org/10.1107/s0567740874007771>

[18] Faust, G. T. (1953). Huntite, $Mg_3Ca(CO_3)_4$ A new mineral. *American Mineralogist: Journal of Earth and Planetary Materials*, 38(1-2), 4-24.

[19] Graf, D. L., & Bradley, W. F. (1962). The crystal structure of huntite, $Mg_3Ca(CO_3)_4$. *Acta Crystallographica*, 15(3), 238–242. <https://doi.org/10.1107/s0365110x62000584>

[20] Murdoch, J. (1954). Unit cell of hydromagnesite. *American Mineralogist: Journal of Earth and Planetary Materials*, 39(1-2), 24-29.

[21] Rogers, A. F. (1923). The crystallography of hydromagnesite. *American Journal of Science*, s5-6(31), 37–47. <https://doi.org/10.2475/ajs.s5-6.31.37>

[22] Beck, C. W. (1950). Differential thermal analysis curves of carbonate minerals. *American Mineralogist: Journal of Earth and Planetary Materials*, 35(11-12), 985-1013.

[23] Botha, A., & Strydom, C. (2003). DTA and FT-IR analysis of the rehydration of basic magnesium carbonate. *Journal of Thermal Analysis and Calorimetry*, 71(3), 987-996.

[24] Botha, A., & Strydom, C. A. (2001). Preparation of a magnesium hydroxy carbonate from magnesium hydroxide. *Hydrometallurgy*, 62(3), 175-183.

[25] Choudhary, V. R., Pataskar, S. G., Gunjekar, V. G., & Zope, G. B. (1994). Influence of preparation conditions of basic magnesium carbonate on its thermal analysis. *Thermochimica acta*, 232(1), 95-110. [26] Vágvölgyi, V., Frost, R. L., Hales, M., Locke, A., Kristóf, J., & Horváth, E. (2008). Controlled rate thermal analysis of hydromagnesite. *Journal of Thermal Analysis and Calorimetry*, 92, 893-897.

[27] Haurie, L., Fernandez, A. I., Velasco, J. I., Chimenos, J. M., Lopez-Cuesta, J. M., & Espiell, F. (2007). Effects of milling on the thermal stability of synthetic hydromagnesite. *Materials Research Bulletin*, 42(6), 1010-1018.

[28] Inglethorpe, S. D. J., & Stamatakis, M. G. (2003). Thermal decomposition of natural mixtures of hydromagnesite and huntite from Kozani, Northern Greece. *Mineral Wealth*, 126, 7-18.

[29] Khan, N., Dollimore, D., Alexander, K., & Wilburn, F. W. (2001). The origin of the exothermic peak in the thermal decomposition of basic magnesium carbonate. *Thermochimica Acta*, 367, 321-333.

[30] Ozao, R., & Otsuka, R. (1985). Thermoanalytical investigation of huntite. *Thermochimica acta*, 86, 45-58.

[31] Padeste, C., Oswald, H. R., & Reller, A. (1991). The thermal behaviour of pure and nickel-doped hydromagnesite in different atmospheres. *Materials research bulletin*, 26(12), 1263-1268.

[32] Rajeswara R, Chohan VS. Kinetics of thermal decomposition of hydromagnesite. *Chem Eng Technol* 1995;18:359e63.

[33] Sawada, Y., Uematsu, K., Mizutani, N., & Kato, M. (1978). Thermal decomposition of hydromagnesite $4\text{MgCO}_3 \cdot \text{Mg}(\text{OH})_2 \cdot 4\text{H}_2\text{O}$. *Journal of Inorganic and Nuclear Chemistry*, 40(6), 979-982.

[34] Sawada, Y., Uematsu, K., Mizutani, N., & Kato, M. (1978). Thermal decomposition of hydromagnesite $4\text{MgCO}_3 \cdot \text{Mg}(\text{OH})_2 \cdot 4\text{H}_2\text{O}$ under different partial pressures of carbon dioxide. *Thermochimica acta*, 27(1-3), 45-59.

[35] Sawada, Y., Yamaguchi, J., Sakurai, O., Uematsu, K., Mizutani, N., & Kato, M. (1979). Thermal decomposition of basic magnesium carbonates under high-pressure gas atmospheres. *Thermochimica acta*, 32(1-2), 277-291.

[36] Sawada, Y., Yamaguchi, J., Sakurai, O., Uematsu, K., Mizutani, N., & Kato, M. (1979). Thermogravimetric study on the decomposition of hydromagnesite $4\text{MgCO}_3 \cdot \text{Mg}(\text{OH})_2 \cdot 4\text{H}_2\text{O}$. *Thermochimica acta*, 33, 127-140.

[37] Sawada, Y., Yamaguchi, J., Sakurai, O., Uematsu, K., Mizutani, N., & Kato, M. (1979). Isothermal differential scanning calorimetry on an exothermic phenomenon during thermal decomposition of hydromagnesite $4\text{MgCO}_3 \cdot \text{Mg}(\text{OH})_2 \cdot 4\text{H}_2\text{O}$. *Thermochimica Acta*, 34(2), 233-237.